4

GL-TR-89-0287

Polar BEAR UV Imaging of Airglow and Aurora - Imaging Processing and Results

Moshe Tur
Israel Oznovich
Arnoldo Ravitz

Tel Aviv University/Ramot Ltd
Faculty of Engineering
Ramat Aviv
Tel Aviv 69978, ISRAEL

24 September 1989

Final Report
September 1987-August 1989

APPROVED FOR PUBLIC RELEASE; DISTRIBUTION UNLIMITED

GEOPHYSICS LABORATORY
AIR FORCE SYSTEMS COMMAND
UNITED STATES AIR FORCE
HANSCOM AIR FORCE BASE, MASSACHUSETTS 01731-50001

"This technical report has been reviewed and is approved for publication"

F P DelGreco

FRANCIS P. DEL GRECO
Laboratory Contract Manager
Ionospheric Modelling & Remote
Sensing Branch

David N. Anderson

DAVID N. ANDERSON, Acting Branch Chief
Ionospheric Modelling & Remote
Sensing Branch
Ionospheric Physics Division

FOR THE COMMANDER

ROBERT A. SKRIVANEK, Director
Ionospheric Physics Division

This report has been reviewed by the ESD Public Affairs Office (PA) and is releasable to the National Technical Information Service (NTIS).

Qualified requestors may obtain additional copies from the Defense Technical Information Center. All others should apply to the National Technical Information Service.

If your address has changed, or if you wish to be removed from the mailing list, or if the addressee is no longer employed by your organization, please notify GL/IMA, Hanscom AFB, MA 01731. This will assist us in maintaining a current mailing ist.

Do not return copies of this report unless contractual obligations or notices on a specific document requires that it be returned.

UNCLASSIFIED
SECURITY CLASSIFICATION OF THIS PAGE

REPORT DOCUMENTATION PAGE

1a REPORT SECURITY CLASSIFICATION
Unclassified

1b. RESTRICTIVE MARKINGS

2a SECURITY CLASSIFICATION AUTHORITY

2b. DECLASSIFICATION / DOWNGRADING SCHEDULE

3 DISTRIBUTION / AVAILABILITY OF REPORT
Approved for public release;
Distribution unlimited

4. PERFORMING ORGANIZATION REPORT NUMBER(S)

5 MONITORING ORGANIZATION REPORT NUMBER(S)
GL-TR-89-0287

6a. NAME OF PERFORMING ORGANIZATION
Tel Aviv University / Ramot Ltd.

6b. OFFICE SYMBOL *(If applicable)*

7a. NAME OF MONITORING ORGANIZATION
European Office of Aerospace Research & Development

6c. ADDRESS *(City, State, and ZIP Code)*
Faculty of Engineering
Ramat Aviv
Tel-Aviv 69978, Israel

7b ADDRESS *(City, State, and ZIP Code)*
Box 14
EPO New York 09510-0200

8a. NAME OF FUNDING / SPONSORING ORGANIZATION Air Force Geophysics Laboratory

8b OFFICE SYMBOL *(If applicable)*
AFGL/LIU

9 PROCUREMENT INSTRUMENT IDENTIFICATION NUMBER
F49620-87-C-0091

8c. ADDRESS *(City, State, and ZIP Code)*
Hanscom AFB, MA 01731-5000

10. SOURCE OF FUNDING NUMBERS

PROGRAM ELEMENT NO.	PROJECT NO.	TASK NO.	WORK UNIT ACCESSION NO.
62101F	4643	11	AB

11 TITLE *(Include Security Classification)*
Polar BEAR UV Imaging of Airglow and Aurora - Image Processing and Results

12 PERSONAL AUTHOR(S) Moshe Tur, Israel Oznovich and Arnoldo Ravitz

13a TYPE OF REPORT
Final Technical

13b. TIME COVERED
FROM Sept 87 TO Aug 89

14. DATE OF REPORT (Year, Month, Day)
1989 09 24

15. PAGE COUNT
66

16 SUPPLEMENTARY NOTATION

17 COSATI CODES

FIELD	GROUP	SUB-GROUP

18 SUBJECT TERMS *(Continue on reverse if necessary and identify by block number)*
Aurora, airglow, ultraviolet, image processing, Polar BEAR satellite

19 ABSTRACT *(Continue on reverse if necessary and identify by block number)*

In late 1986, AFGL launched the Polar BEAR satellite, which was designed for UV imagery of the northern pole region. The AIRS scanning ultraviolet photometer aboard the satellite provides images of day and night auroral structures of unprecedented spectral and spatial resolution at 2 working spectral windows simultaneously.

It is necessary to apply geometric and photometric corrections to the image in order to enhance and map it onto the ionosphere. Furthermore, satellite attitude corrections are imperative to assure that image coordinates are properly rotated to the real-time body reference system. To the best knowledge of the authors, this project is the first one to fully include geometric and photometric corrections to VUV images of the ionosphere.

20. DISTRIBUTION / AVAILABILITY OF ABSTRACT
☒ UNCLASSIFIED/UNLIMITED ☐ SAME AS RPT ☐ DTIC USERS

21 ABSTRACT SECURITY CLASSIFICATION
Unclassified

22a NAME OF RESPONSIBLE INDIVIDUAL
Francis DelGreco

22b. TELEPHONE *(Include Area Code)*

22c. OFFICE SYMBOL
GL/LIU

DD FORM 1473, 84 MAR

83 APR edition may be used until exhausted.
All other editions are obsolete.

SECURITY CLASSIFICATION OF THIS PAGE
UNCLASSIFIED

In the geometric processing stage, the image is rectified by a transformation which is a function of the instantaneous satellite attitude angles. The geographic location of each pixel within the image is located by tracing the satellite line-of-sight to the height of the emitting layer.

The photometric processing enhances the image in order to make use of the full dynamic range afforded by the image processing hardware. We developed a novel approach toward the separation of dayglow from aurora. The technique is based on a spatially variable intensity criteria. The dayglow intensity in every single image is fitted by a general function. Variables of this function are the solar zenith angle, and the path length of the emitting layer. Pixels with an intensity larger than that function are defined as auroral ones.

The imaging method employed by the satellite creates a space oblique mercator projection of the ionospheric north pole region. The output of the image processing package is an image enhanced and warped to corrected geomagnetic polar stereographic projection.

We have analysed the errors inherent in the image processing techniques. The angular error increases with scan angle. It is larger than 1 degree for scan angles larger than 60 degrees. In the worst case, an average error of 2 degrees exists for a pixel located at a scan angle of 60 degrees.

The error simulation results showed that we can give an upper limit of 1 degree on the error anywhere in the image if we limit the mapping to scan angles that correspond to satellite nadir angles less than 55 degrees.

A set of maps of auroral frequency and average intensity in the ultraviolet, ordered by magnetic activity, has been created. It is the VUV improved version of the well-known Feldstein's oval set. These sets are commonly used in comparative auroral studies.

In the future, the semiautomatic nature of the image-processing routines will allow us to enlarge the small sample (about 40 scenes) to create a statistically valid database (about 50 scenes per Kp group) for the above maps.

Contents

List of Tables

List of Figures

.1 Introduction

The advantage of the far ultraviolet radiation in the investigation of airglow and aurora is that pure absorption is strong enough to prevent the radiation from penetrating to depths where rayleigh scattering, ground and cloud albedo, and scattering from aerosols can take place.

The USAF Geophysics Laboratory has developed and flown the first instrumentation designed for UV imagery with high spatial and wavelength resolution. The AIM scanner flown on the HILAT satellite provided the earliest data showing airglow and auroral morphology and emission processes. HILAT returned a number of images in 1983 with a $30\AA$ spectral resolution and 5×20 *km* spatial resolution. The AIM instrumentation aboard HILAT has been described in several references ([5], [8], [11], and [17]).

In late 1986, AFGL launched a second satellite with similar but improved instrumentation ([2], and [18]). The Polar BEAR satellite has been designed for UV imagery with high spatial and wavelength resolution. The satellite carries the AIRS scanning ultraviolet photometer providing several simultaneous spectral images. These images represent the integrated column photon count of several different upper-atmosphere species. The data stream is currently converted to images representing 5000×5000 *km* records of intensity.

The records of intensity obtained by the Polar BEAR satellite become meaningful results only by manipulating them by image processing techniques.

Previous research by our group, originally led by the late Prof. N. Rosenberg, has laid the foundations for the photometric and geometric processing of both the AIM and the AIRS instruments ([12], [13], [14], [15], and [16]).

A software package has been developed to process large number of images supplied by the AIRS instrument. The package transforms the time-spaced data stream to a photometrically and geometrically standardised image in a semiautomatic manner.

Table 1 presents a summary of programs and procedures newly developed or updated in the course of this research. A data-flow diagram for basic image processing of the AIRS pictures is shown in Figure 1. The flowsheet shows processes, and the relations between them. A single scene is defined as a multidetector record for a given site, day, and pass.

name	*description*
amov	automatic image moving procedure (screen to screen, screen to file, and vise versa)
attitude	fit an offset sinsuidal function $\Theta(t)$ to attitude angles; extrapolate Θ to fill-in null pitch, yaw, and roll
aurlsq	search for auroral brightness correlation with path length
aurmean	average multiple auroral images; produces multiple image-coverage, auroral frequency, and average intensity
aurplot	plot image upon corrected geomagnetic coordinate system
chapman	Chapman function $Ch(\chi, X)$ for $65° \leq \chi \leq 105°$, $X = 170$
circle	draws a circle of chosen color and radius on screen
circum	plot image circumference (field-of-view)
compraw	compare two orbital data files
corrgm	corrected geomagnetic lat, lon for geographic lat, lon
craur	fit a circle to maximum auroral brightness
detc	mode-smooth, amplify, filter, and warp image
dipgm	dipole geomagnetic lat, lon for geographic lat, lon
distance	distance image of object to background and vise versa
edgim	find smallest rectangle bounding image
frame	sketch border lines on screen
geomlsq	correlate dayglow intensity with path length and χ; subtract fitted background dayglow from warped image

Table 1: Basic Software Package

name	*description*
gmcoord	overlay geographic or geomagnetic grid upon image
grafaur	graph auroral intensity versus magnetic latitude, local-time, or pixel distance
grafile	graph any ascii [illegible] with integer pairs on screen
grafim	graph image histogram, or (average) line/column brightness
ht	halftone image from byte to bit
ht2hp	printer utility - halftone to laser printer (hp)
ht2pr	printer utility - halftone to matrix printer (epson)
imfair	get Interplanetary Magnetic Field data for AIRS image
integrate	integrate image brightness
landmass	overlay geographic grid and/or landmass features on image
latoval	plot polar corrected geomagnetic latitude—magnetic local-time coordinate system and/or Feldstein's oval
linlsq	linear least-squares fit to n data points for m unknowns
list	list orbital data summary of multiple orbital files
med	calculate attitude parameters statistics
medfill	automatic procedure for filling-in image with median filter
monthday	month and day from year and day number
mulbnd	two-color output image from two input detectors
newscl	re-scales image brightness
overlim	overlay one image on another

Table 1: Basic Software Package (cont)

name	*description*
plattit	graph attitude parameter pitch, yaw, or roll versus time
pllat	automatic procedure to plot geomagnetic latitude lines
plotgm	draw dipole or corrected geomagnetic grid upon image
plovlat	interactively plot coordinate system and auroral oval
pl_graf	automatic procedure to graph two integer vectors on screen
rawcvt	convert raw ascii file to binary image + orbital data file
replsq	report least-squares fit data of multiple images
rewarp	interactive program to re-warp raw image
rhline_p	emulate PC integer size to μVax integer size
rhline_v	emulate FG100AT procedures to IP-512 driver software
scene	calculate orbital, geometrical, and geophysical parameters
stdsubs	standard subroutines, including Euler's rotation matrix
sundec	sun declination from date and time
terminator	mark sun terminator on an image mapped by either geomagnetic or geographic coordinates
warpm	automatic procedure to warp an image with error control
xmov	interactive image moving program (screen to screen, screen to file, and vise versa)
zoomfil	zoom image file to image file (in multiples of 2)
zoomim	magnify image on screen

Table .1: Basic software package. (cont)

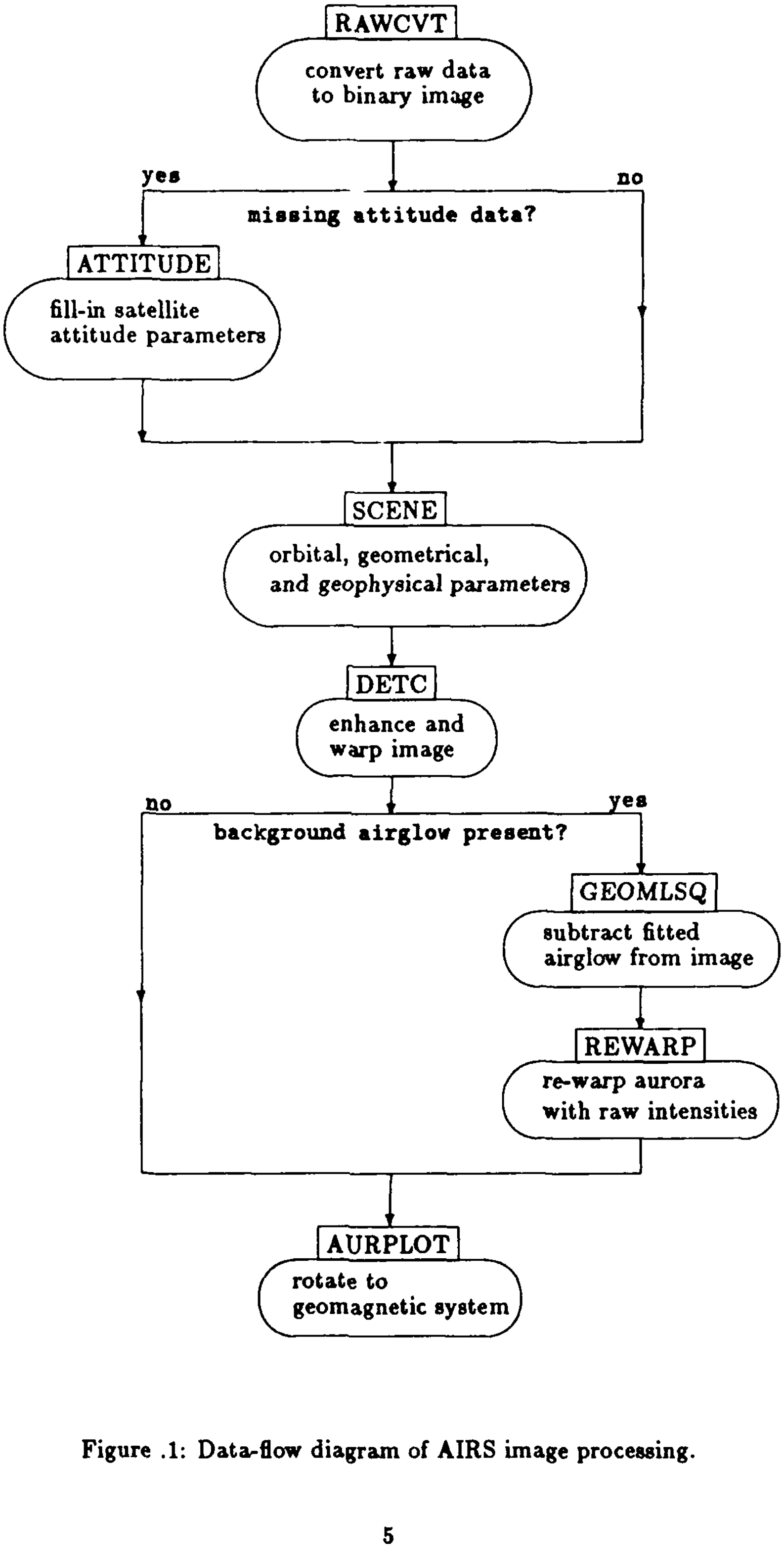

Figure .1: Data-flow diagram of AIRS image processing.

.2 Pre-processing

.2.1 Raw Data Structure

The Polar BEAR satellite cruises at an altitude of approximately 1000 kilometers at an inclination angle of 89.56 degrees to the equator, i.e. in a nearly polar orbit.

The Auroral Ionospheric Remote Sensor (AIRS) is the prime instrument onboard the three-axis stabilised craft. AIRS provides 326 samples of emission count in an angular scan from $-65.2°$ to $+65.2°$ perpendicular to the satellite orbit. The scan cycle is completed in 3 seconds and a typical 11 minutes recording provides $\sim$ 220 scan lines.

AIRS acquires a single scene per orbit at the two working wavelengths (1356Å, and 1596Å). Each pixel, which is equivalent to a mirror step, has an integration time of 6.83 milliseconds, and a readout time of 0.2 msec.

The VUV Instantaneous Field Of View (IFOV) is $0.373° \times 1.53°$. Raw image structure is summarised in Figure 2, in which each ellipse is a single pixel. Line and column are l and k respectively.

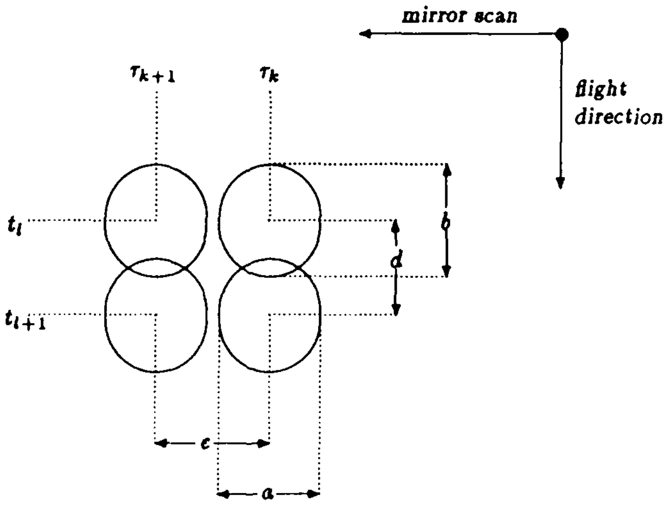

Figure .2: Raw VUV image structure.

The VUV pixels are mapped on an emitting layer 150 *km* above ground. There, the nadir pixels have the following dimensions:

$$\begin{array}{rclcr}
a & = & 0.373^\circ & = & 5.5\ km \\
b & = & 1.53^\circ & = & 22.7\ km \\
c & = & 0.4^\circ & = & 5.9\ km \\
d & = & 1.3^\circ & = & 19.3\ km \\
\Delta t & = & t_{l+1} - t_l & = & 3\ \ sec \\
\Delta \tau & = & \tau_{k+1} - \tau_k & = & 7\ msec
\end{array}$$

The spacecraft forward velocity v_s was designed to be 6.6 *km/sec* at ground subtract point. We fitted ground path d to time of flight t via

$$d = d_0 + v_s \cdot (t - t_0)$$

for each scene to find $v_s = 6.3 \pm 0.02$ *km/sec* for all scenes processed so far. This velocity brings about a ground distance of 18.9 *km* between consecutive lines, and a distance of 19.3 *km* between consecutive lines at an altitude of 150 *km*.

Because the satellite platform is not well stabilised, pitch, yaw, and roll corrections to the scan pointing direction must be included. In general scan lines are not parallel, and are not perpendicular to the orbital ground path.

.2.2 Binary Image Preparation

Each raw scan record contains two lines — a data line of 326 valuable intensity values, and a control line with the following data:

- Universal Time (UT) of scan initiation (in seconds).
- Geographic latitude and longitude of satellite nadir.
- Satellite attitude angles: pitch, yaw, and roll.
- Height of satellite above ground (in kilometers).

The initial processing (program RAWCVT) converts a raw ascii file with records as above to two files:

1. A binary image of 240 rows × 240 columns.
2. An ascii file containing 41 lines of orbital data.

The orbital data file contains control lines from the original file for every sixth record. The image is formed by converting ~ 220 lines of numbers to 240 lines of binary data. The number of lines in a raw file varies from 120 to 330, with an average of 220. Lines are either multiplied or skipped upon in order to conform the binary image to the predetermined size. The warping of the image in the post-processing stage eliminates the redundancy in identical lines, as will be shown later. The case of line skipping is extremely rare, as most raw files contain 240 records or less. The program handles data gaps and tests whether the raw data is packed. If packed, procedure UNPAK is invoked to generate a nonsaturated image.

The size of the binary image, a matrix of 240 × 240 pixels, is maintained in order to conform to past work and data files. The resampling of the columns is more complicated than line stretching. This part of the processing has gone a major change since past work, which influences the image structure considerably. Hence it will be discussed separately in the following subsection.

.2.3 Resampling the Raw Line

The raw line contains 336 values, of which the first and last five are null. These two unsampled degrees on each side of the scan line correspond to the fact that the mirror scans through ±67.2 degrees, of which only ±65.2 degrees of data is collected due to telemetry constraints.

Figure 3 shows the resampling of 326 pixels in a raw line to 240 pixels of the output line:

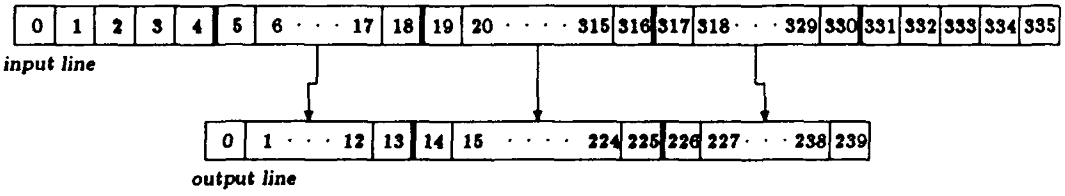

Figure .3: Resampling geometry.

The first and last meaningful 14 pixels (column # 5–18, and 317–330) of the raw line are copied directly to the first and last 14 pixels (column # 0–13, and 226–239) of the output line respectively. These 28 pixels retain their signal and IFOV perpendicular to flight path—0.4°. The inner 298 pixels of the input line are resampled to the inner 212 pixels of the output line.

The differential sampling is due to the fact that we want to maintain maximum resolution at the edges of the image. We use these edge pixels later on to correct the roll of the satellite by adjusting it to the location of the limb.

At the central part of the raw line, we transform each input pixel with an IFOV of 0.4°, to an output pixel with an IFOV of $\frac{298}{212} \cdot 0.4° \simeq 0.56°$.

The poor signal in each pixel drives us to maintain the raw line-integrated intensity. Therefore we redistribute the signal of the inner 298 pixels to 212 pixels with a normalised weighting function.

The redistribution scheme is according to weights proportional to the distance of the designated index to the two closest integers. Let ϱ be the discrete weighting function, i the input index, and j the output index. Then for $i = 19, \ldots, 316$:

$$x = (i - 19) \cdot \frac{211}{297} + 14$$

$$j_i = \lfloor x \rfloor$$

$$\varrho_i = 1 - (x - \lfloor x \rfloor)$$

If IN is the input line, and OUT the output line, then

$$\begin{aligned} OUT_{j_i} &= \sum_{i=19}^{316} IN_i \cdot \varrho_i \\ OUT_{j_i+1} &= \sum_{i=19}^{316} IN_i \cdot (1 - \varrho_i) \end{aligned}$$

A major deficiency of the above weighted redistribution is its nonlinearity, i.e. the sum of weights per output pixel is not exactly constant. The fact that the transfer function is nonlinear implies that the resampling of a constant signal , i.e. a line with a constant value, is not constant.

A linearisation method is introduced in order to normalise the sum of weights of every output index to the actual increase in IFOV ($\frac{298}{212} = 1.406$). If $\hat{\varrho}$ is the desired normalised weighting function, then

$$\begin{aligned} \hat{\varrho}_{j_i} &= \sum_{i=19}^{316} \varrho_i \\ \hat{\varrho}_{j_i+1} &= \sum_{i=19}^{316} (1 - \varrho_i) \end{aligned}$$

and for $j = 14, \ldots, 225$:

$$\hat{\varrho}_j = 1.406 / \hat{\varrho}_j$$

Once the output line has been computed based on the input line, the intensity of each output pixel is normalised to the actual increase in IFOV, via

$$OUT_j = OUT_j \cdot \hat{\varrho}_j$$

Figure 4 shows a typical *OUT* image, as produced by RAWCVT.

Note the relatively low signal that is present in the unstretched image. Count dynamic range is 50, equivalent to a maximum intensity of $\sim 1K$ Rayleighs (1 count ≡ 21 Rayleighs for a pixel with an IFOV of 0.56° at 1356Å).

The raw image is customarily rotated to align north up, east to the right side of the image. Thin auroral arcs inhabit the central part of the image. The scattered radiation at the lower half of the image is twilight and dayglow. Nightglow intensity is below the threshold of the detector, hence no counts are registered in the upper mid-part of the image. Note the brightened limbs, to be discussed in the following section.

Figure .4: Raw image - file s87023h2 (scene 07), detector 2 (λ = 1356Å).

.2.4 Attitude Control

The Polar BEAR is a three-axis stabilised satellite. A sun sensor and a fluxgate magnetometer measure the three angles of the instantaneous position of the satellite relative to the nadir direction. Since one of the craft attitude sensors is a sun sensor, attitude data is available only under sunlight.

On the average, the instantaneous instability of the spacecraft is of order 1–2 degrees in pitch, 2–5 degrees in roll, and 4–11 degrees in yaw. These magnitudes vary with time on a time-scale of weeks to months. Over the entire lifetime of the satellite, these instabilities have caused the satellite to invert to the zenith direction more than once.

At night, no attitude data is available. Almost all images are partly in the earth's shadow. Thus, in principle, each and every image can be partially correctly oriented, partially not. This fact creates a distortion not only between images, but also within a single image.

The null hypothesis is that the satellite points directly downward at the nadir direction. This allows one to assume zero attitude corrections to the three directions in non-sunlit conditions. In light of the above magnitudes of pitch, roll, and especially yaw, as measured in the sunlit hemisphere, we find this limitation quite significant when one tries to find the geographic and geomagnetic coordinates of the image correctly.

In order to be able to correct for the satellite attitude variations when no corresponding data is available, we have embarked on the following:

- Error quantification using a few typical images.
- Study of the Polar BEAR's attitude changes in time.
- Development of an algorithm to solve the problem, in effect stabilising the craft retrospectively.
- Test the statistical validity of the technique.

Error quantification

Obviously, the error in position is minimal in the nadir direction, and maximal in the east and west edges of each line.

We scaled two images, obtained under full sunlight, with and without the attitude corrections as provided by the sun sensor and the magnetometer. The images were chosen to represent data with close to minimum (t8703072—scene 24), and close to maximum (r87051k2—scene 40) attitude corrections. Pitch, roll, and yaw amplitudes in scene 24 were 2°, 3°, and 4° respectively, and 2°, 4°, and 10° respectively in scene 40.

Table 2 shows ground distances x and y (in kilometers) at the edges of the two pairs of data. The cartesian x, y coordinate system is laid on a hypothetical spherical earth. The x-axis is the projection of the satellite track on that sphere; the y-axis is perpendicular to it. The y coordinate is formed by the projection of the instantaneous line-of-sight to the center of the emitting layer (assumed to be at an altitude of 150 *km*), and down to the earth. The origin of the coordinate system, i.e. $(x, y) = (0, 0)$, is at the nadir location of the satellite at first-line acquisition time.

scene 24											
without attitude corrections						with attitude corrections					
x			y			x			y		
2	0	-4	-1968	0	1960	-49	-15	5	-1967	-19	1968
1852	1849	1844	-1982	0	1982	1942	1824	1680	-1980	-14	1976
3702	3699	3695	-1998	0	1998	3698	3685	3659	-1998	-15	1997
scene 40											
without attitude corrections						with attitude corrections					
x			y			x			y		
1	-1	-5	-2014	0	2014	-408	-25	335	-1978	1	1990
2104	2101	2096	-2023	0	2023	2002	2070	2108	-2020	13	2023
4206	4203	4199	-2028	0	2028	4390	4175	3935	-2021	0	2013

Table .2: Influence of attitude corrections on ground distances (in *km*).

For the best case, i.e. scene 24, the averaged central x and y distances differ by 18 and 16 kilometers, corresponding to $\sim$1, and $\sim$3 VUV pixels respectively. At the edges, x and y distances without attitude corrections differ from the distances that include attitude corrections by as much as 47 and 70 kilometers respectively.

By contrast, scene 40 exhibits differences of up to 200 kilometers in the x-axis at the edges, and similar errors in the central pixels. The greater error in the x distances relative to the y distances is due to a large yaw correction.

The conclusion is therefore that the error in pixel localisation when using an image lacking attitude data is significant even for cases where pitch, roll, and yaw are 2–5°, and even at the central part of the image. If large ($\geq 10°$) attitude corrections are in order, the error per pixel is of order 100–300 kilometers at the edges, and tapers off to a few dozens of kilometers at the center.

Temporal attitude behavior

Rosenberg and Quesada ([16]) noted that the Polar BEAR satellite changes its attitude in a periodic fashion. We have found this periodicity to sustain (with increasing amplitude in time) over the first half year of Polar BEAR's life in orbit by plotting a few dozen passes randomly chosen from that era.

Figure 5 shows the temporal evolution of the three attitude angles for scene 40, as extracted from file r87051k2:

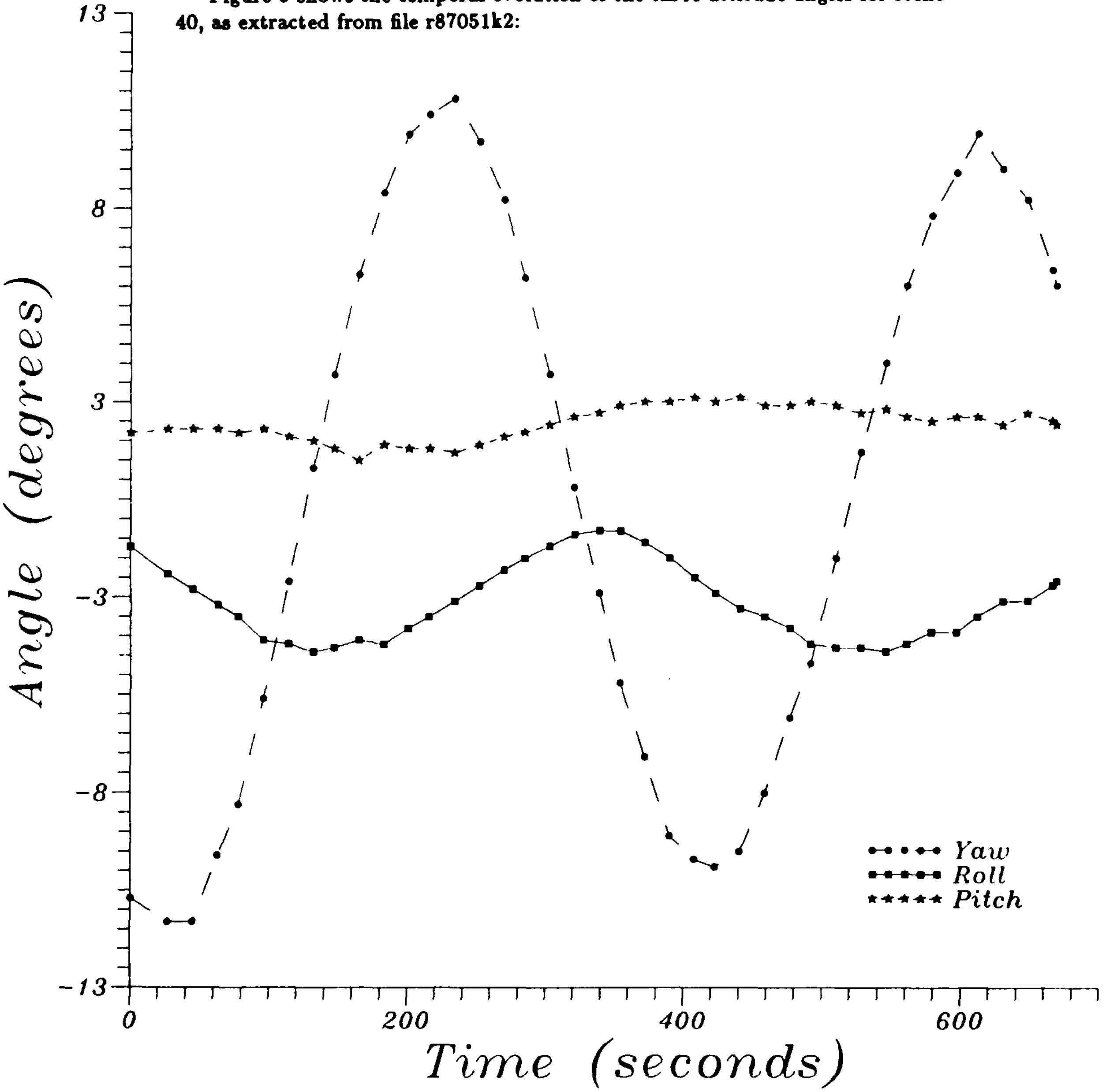

Figure .5: Attitude angles versus time - scene 40.

The pitch, yaw, and roll angles of the satellite vary periodically with time. The temporal behavior of the three attitude angles can be approximated by an offset sine function:

$$\Theta(t) = A_\Theta \cdot \sin(w_\Theta \cdot t + \phi_\Theta) \ + \ \Theta(0)$$

where the attitude angle Θ, as a function of time t, depends on four variables: A_Θ - amplitude, w_Θ - frequency, ϕ_Θ - phase, and $\Theta(0)$ - offset.

By fitting all four parameters independently to several scenes, we found that the function describes the three angles well. Hence it seems reliable to describe the motion of the satellite around three orthogonal axes by above function.

Periodic attitude extrapolation

The amplitude, phase, frequency, and offset magnitudes change slowly in time (on a time-scale of weeks to months). Hence we devised the following algorithm to extrapolate daytime attitude corrections to nighttime. The method can be applied within a certain scene, or between two different scenes closely spaced in time.

An offset sinusoidal is fitted to attitude data as reported by the two sensors in the day side part of the image. The extrapolated coefficients are used to fill-in the missing attitude data for the nighttime part of the scene. The extrapolation for a scene with very little or no attitude data at all is performed based on data from another scene with sufficient attitude information. Sufficient data is defined to be a data set with a time span larger than half a period ($P_\Theta = \frac{2\cdot\pi}{w_\Theta}$). The scene from which the parameters are established from should be temporally close to the designated scene as possible, and never more than a few days apart.

Figure 6 shows an application of the self-extrapolation technique on the yaw data (program ATTITUDE). Bar histogram line shows original data, smooth line is the fitted and extrapolated one. The plot itself was produced by PLATTIT. Scene 54 (file s8705992) was used to produce the results shown in Figure 6 and the following table. In this least-squares fit a free choice of frequency for every attitude angle was allowed. The resultant periods are 395.2, 390.3, and 395.2 seconds for yaw, roll, and pitch respectively. These results support Rosenberg and Quesada's ([16]) statement regarding the coupling between the three angles.

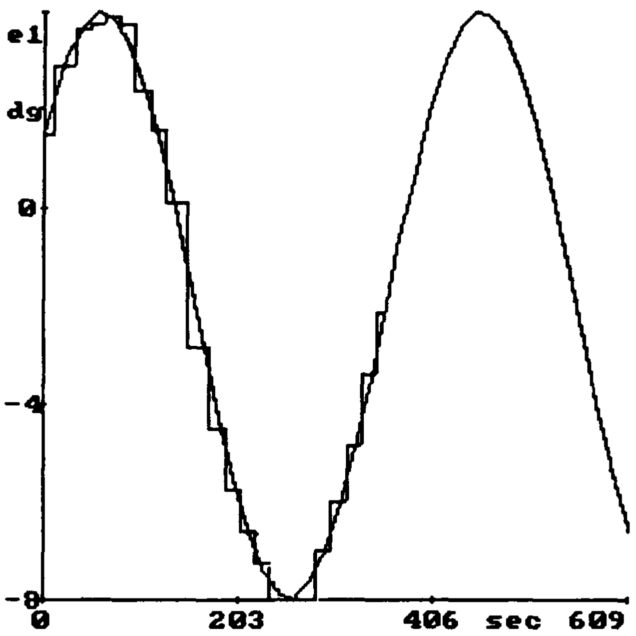

Figure .6: Yaw data extrapolation - scene 54.

attitude angle	A_Θ amplitude *(degrees)*	P_Θ period *(seconds)*	ϕ_Θ phase *(degrees)*	$\Theta(0)$ offset *(degrees)*
yaw	7.5	395.2	51.8	0.4
roll	1.0	390.3	-53.1	-2.3
pitch	0.6	395.2	-123.8	1.2

Table .3: Determined variables of the attitude self-extrapolation technique.

Statistical tests

We took the following steps in order to test the validity of the above technique:

- Choose two scenes, closely spaced in time, both taken under sunlit conditions; the two scenes then contain complete, or almost complete attitude information.
- Use one scene's data to extrapolate pitch, roll, and yaw to the second scene and vise-versa; the result will be two pairs of data sets, corresponding to the two scenes; each pair includes the actual attitude angles and the extrapolated ones.

- Perform a statistical comparison of each pair to find the correlation coefficient between the actual and the calculated attitude angles.

Ideally the two sets of data should match, and we should get a perfect correlation ($r = 1$) between the two sets. If the extrapolated values differ from the actual ones significantly, the coefficient of correlation r should be low or insignificant according to the t test.

Table 4 presents the results of a test of this nature performed by program COMPRAW between scene 06 and scene 07. The dates and times of the two scenes are: scene 06 - year 87 - day 47 - start time 43229.15 seconds, and scene 07 - year 87 - day 48 - start time 51323.15 seconds.

File 1 contains the raw data, file 2—the calculated data. Notation of statistical parameters is as follows: μ_Θ - arithmetic mean, $\bar{\sigma}_\Theta$ - mean deviation, σ_Θ - standard deviation, $100 \cdot \frac{\sigma_\Theta}{\mu_\Theta}$ - coefficient of variation, $S_{\Theta_1|\Theta_2}$ - standard error of the estimate, r - coefficient of correlation, and t - t test.

scene	Θ	file#	μ_Θ	$\bar{\sigma}_\Theta$	σ_Θ	$100 \cdot \frac{\sigma_\Theta}{\mu_\Theta}$	$S_{\Theta_1\|\Theta_2}$	r	t
06	yaw	1	0.76	5.03	5.69	113.07%			
		2	1.06	5.37	6.03	112.26%			
		1↔2					1.53	0.97	23.73
	roll	1	-3.00	0.67	0.77	25.73%			
		2	-2.53	0.74	0.82	32.33%			
		1↔2					0.57	0.92	14.70
	pitch	1	1.17	0.27	0.33	28.35%			
		2	1.99	0.28	0.31	15.71%			
		1↔2					0.85	0.77	7.27
07	yaw	1	1.27	5.19	5.91	113.96%			
		2	1.51	4.75	5.43	114.34%			
		1↔2					2.56	0.90	12.03
	roll	1	-2.64	0.77	0.85	32.09%			
		2	-2.87	0.64	0.70	24.48%			
		1↔2					0.41	0.92	13.67
	pitch	1	1.97	0.44	0.52	26.16%			
		2	1.14	0.24	0.27	23.54%			
		1↔2					0.94	0.50	3.33

Table .4: Actual and extrapolated attitude angles - a statistical comparison.

Note that $t > 3.5$ implies a level of significance P of null hypothesis (Θ_1 and Θ_2 are uncorrelated) of 0.001, hence the value of r is significant!

The results of the above test clearly indicate an excellent agreement between the actual parameters and the extrapolated ones. The value of the coefficient of correlation is above 90% for yaw and roll. It is lower for the pitch angle since its amplitude is relatively small. It is comparable, in fact, to the 1–2° error measurement of these angles by the attitude sensors.

.3 Geometric Processing

.3.1 Motivation

Geometric corrections are applied to the image in order to rectify and map it onto the ionosphere. Furthermore, satellite attitude corrections are imperative to assure that image coordinates are properly rotated to the real-time body reference system. To the best knowledge of the authors, this project is the first one to fully include geometric and photometric corrections to VUV images of the ionosphere.

The geometric corrections include the following:

- A correction to the satellite roll based on the dayglow limbs observed at the edges of the image.
- Image rectification via a transformation which is a function of the instantaneous satellite attitude angles.
- The geographic location of each pixel within the image is located by tracing the satellite line-of-sight to the height of the emitting layer.

.3.2 Roll Adjustment

Evident from the raw image shown in Figure 4, the east and west edges of the image are typified by an intensity enhancement.

Assume that the ionospheric region contributing to the airglow intensity has a constant thickness. If the emission is optically thin, then the above phenomenon is easily explained by limb brightening. Even if some multiple scattering effects cause this phenomenon, it is still clear that it is path length dependent.

Hence we receive an increased radiation as the mirror scans from local nadir to the horison. All other parameters constant, the maximum intensity will be at the point where the length of the emitting layer, relative to the detector, is maximum.

Since *not* all the other parameters equal, the limb enhancement occurs unevenly for the two sides of the image. In Figure 4, for example, the sun is located toward the southeast edge of the image, making the east (right) limb brighter than the west (left) one.

Based on the above, we use the brightest limb that is present in the image to correct for the satellite roll. Roll adjustment is performed in three steps:

1. The brightest limb in the image is chosen according to its angular proximity to the sun.
2. Search for the brightest column in every image line in the neighborhood of the chosen edge. A linear interpolation is performed in order to fill-in column numbers for unsuccessful lines. The search itself is under a continuity restraint, i.e. column numbers in successive lines can differ by 2 pixels at the most.
3. The adjustment to satellite roll per image line is the difference between the scan angle that corresponds to the column number of maximum intensity, and the scan angle that corresponds to a line-of-sight tangent to the emitting layer.

The roll adjustment is performed only on limbs under dayglow radiation, i.e. for solar zenith angles $\chi \leq 88°$. The theoretical scan angle of line-of-sight tangent to the center of the emitting layer is geometrically computed using a Chapman approximation to limb height h:

$$h = 160 - 25 \cdot \log_{10}(\cos \chi)$$

see also Strickland and Anderson ([20]).

The following table lists the average roll adjustment of a few scenes with corresponding solar zenith angles (χ) at the center of the image.

scene #	χ at image center	roll adjustment
06	88.0	1.9 ± 0.3
07	92.4	1.5 ± 0.2
32	96.0	1.8 ± 0.2
33	96.4	1.9 ± 0.3
34	80.5	1.5 ± 0.3
35	84.3	1.7 ± 0.4
36	86.5	1.6 ± 0.8
37	84.6	1.5 ± 0.3
38	87.7	1.4 ± 0.4
40	90.5	1.2 ± 0.4
57	89.2	1.2 ± 0.4
59	90.6	1.2 ± 0.4

Table .5: Average roll adjustment.

For a specific scene, the roll may vary by as much as 3°, whereas the roll adjustment has a dynamic range of $\sim 1°$.

Since something like a minimum intensity criteria ($\chi \leq 88°$) is imposed on the brightness of the limb in order to initiate this procedure, it is clear that images obtained at local midnight will have no roll adjustment. Major parts of the north polar region experience continuous darkness during the winter. That implies that quite a few images at that time will lack the roll correction.

Notice, however, that the average roll adjustment per scene, as listed in table 5, is quite constant. The variation of the average roll adjustment between scenes is, in fact, much smaller than both the variation of the roll and the roll adjustment within a certain scene. It may be that the attitude sensors have a constant offset of its readings. Thus we apply a constant roll adjustment of 1.6° in case the roll adjustment procedure may not be applied.

.3.3 Basic Geometry

Figure 7 shows satellite - earth geometry as used in this project. The satellite cruises at an altitude of H_s kilometers above ground. The ionospheric emitting layer responsible for the intensity measured by the satellite lies between altitudes h_1 and h_2, with thickness $\Delta h = h_1 - h_2$. We use $h = < h_1, h_2 >$ as the actual height of the emitting layer for pixel localisation.

Satellite reference system is represented by the (X_s, Y_s, Z_s) coordinate system. X_s is the roll axis, Y_s the pitch axis, and Z_s - the yaw axis. Scan angle is measured from Z_s on the Y_sZ_s plane.

The reference coordinate system is (X, Y, Z). Its X-axis is directed toward v_s, the satellite velocity vector. The Z-axis originates within the satellite and is directed toward earth's center. The Y-axis complements a right-handed system. The reference coordinate system follows the motion of the satellite in its orbit.

In general, one wishes to find the coordinates of pixels within the image in a geocentric coordinate system. Two transformations are required :

- From the body (satellite) coordinate system to a reference system.
- From the reference system to a geocentric system, which is (almost) inertial.

Vector $\vec{l}$, in the (X_s, Y_s, Z_s) coordinate system, points toward the instantaneous line-of-sight. It has an angle α to Z_s, α being the scan angle. Vector $\vec{p}$, in the (X, Y, Z) coordinate system, has an angle of α' degrees to the Z axis. It is a transformation of $\vec{l}$ via :

$$\vec{p} = \mathbf{A} \cdot \vec{l}$$

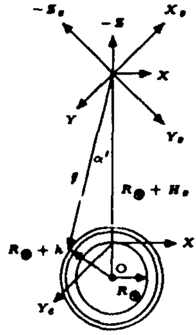

Figure .7: Satellite - Earth geometry.

where

$$\vec{p} = \begin{pmatrix} 0 \\ \sin\alpha' \\ \cos\alpha' \end{pmatrix} \qquad \vec{l} = \begin{pmatrix} 0 \\ \sin\alpha \\ \cos\alpha \end{pmatrix}$$

Following Sommerville ([19]), $\mathbf{A} = (a_{ij})$ is Euler's general rotation matrix :

$$\begin{aligned}
a_{11} &= \cos\Omega + \frac{R^2}{\Omega^2}\cdot(1-\cos\Omega) \\
a_{12} &= \frac{Y}{\Omega}\cdot\sin\Omega + \frac{P\cdot R}{\Omega^2}\cdot(1-\cos\Omega) \\
a_{13} &= -\frac{P}{\Omega}\cdot\sin\Omega + \frac{R\cdot Y}{\Omega^2}\cdot(1-\cos\Omega) \\
a_{21} &= -\frac{Y}{\Omega}\cdot\sin\Omega + \frac{P\cdot R}{\Omega^2}\cdot(1-\cos\Omega) \\
a_{22} &= \cos\Omega + \frac{P^2}{\Omega^2}\cdot(1-\cos\Omega) \\
a_{23} &= \frac{R}{\Omega}\cdot\sin\Omega + \frac{P\cdot Y}{\Omega^2}\cdot(1-\cos\Omega) \\
a_{31} &= \frac{P}{\Omega}\cdot\sin\Omega + \frac{R\cdot Y}{\Omega^2}\cdot(1-\cos\Omega) \\
a_{32} &= -\frac{R}{\Omega}\cdot\sin\Omega + \frac{P\cdot Y}{\Omega^2}\cdot(1-\cos\Omega) \\
a_{33} &= \cos\Omega + \frac{Y^2}{\Omega^2}\cdot(1-\cos\Omega)
\end{aligned}$$

with $\Omega^2 = R^2 + P^2 + Y^2$, and R, P, and Y as the roll, pitch, and yaw angles respectively.

The length of the vector $\vec{p}$, i.e. p, is the distance between the satellite and the emitting layer at an altitude of h kilometers above ground for the instantaneous scan angle α :

$$p = (R_\oplus + H_s)\cdot\cos\alpha' - \sqrt{(R_\oplus + H_s)^2\cdot\cos^2\alpha' - (R_\oplus + H_s)^2 + (R_\oplus + h)^2}$$

The vertex of the angle β is O, earth's center. It is the angle between $-Z$ and the vector from O to the point at which $\vec{p}$ is tangent to the emitting layer :

$$\beta = \arcsin\left(\frac{\sqrt{p_x^2 + p_y^2}}{R_\oplus + h}\right)$$

.3.4 Image Ground Coordinates

The (X_e, Y_e) system (see Fig. 7) is a 2-D cartesian coordinate system on the surface of a spherical earth. The X_e axis is the projection of the satellite track on the ground. The Y_e is perpendicular to it. The origin of the system is at the ground projection of the satellite location at first-line acquisition time.

The coordinates X_e and Y_e are ground distances. Y_e is the distance of the projection of the scan line-of-sight to satellite nadir. X_e is the ground distance of the instantaneous satellite nadir point to the position of the first line parallel to the projected satellite track.

Y_e and X_e are given by the solution of a spherical triangle :

$$\begin{aligned} X_e &= R_\oplus \cdot \arctan(\cos \Upsilon \cdot \tan \beta) \\ Y_e &= R_\oplus \cdot \arcsin(\sin \Upsilon \cdot \sin \beta) \end{aligned}$$

where Υ is the angle between the projection of $\vec{p}$ on the $X-Y$ plane and the X axis.

The geographic latitude (ϕ) and longitude (λ) of the projection of each pixel on the emitting layer can be computed via its X_e, Y_e coordinates. Let

$$\Theta = \frac{Y_e}{R_\oplus} \qquad \sigma = \sigma_0 + \frac{X_e}{R_\oplus}$$

and get ϕ and λ as a function of Θ and σ:

$$\begin{aligned} \sin \phi &= \frac{\sin i \cdot \sin \sigma + \Theta \cdot \cos i}{\sqrt{1+\Theta^2}} \\ \tan \lambda &= \frac{\tan \lambda_0 \cdot \cos \sigma + \cos i \cdot \sin \sigma - \Theta \cdot \sin i}{\cos \sigma - \tan \lambda_0 \cdot \cos i \cdot \sin \sigma + \Theta \cdot \tan \lambda_0 \cdot \sin i} \end{aligned}$$

The inclination of the orbit is i. λ_0 is the geographic longitude of the orbit at the equator. σ_0 is the angular distance (on the ground) between the orbital intersection with the equator and the origin of X_e, Y_e.

.3.5 Image Rectification

The ground mapping of pixels on the X_e, Y_e coordinate system is performed only for certain scan angles. A scan angle must be in the range of the east and west scan angles that are tangent to the spherical ground earth. Other scan angles are ambiguous in its ground locations, since its line-of-sights crosses the center of the emitting layer more than once.

The mapping is performed on 41 equally spaced scan angles. Thus a 41×41 matrix is mapped on the surface of the earth. Each 4 point cell of the above matrix is used for a bi-linear interpolation of all 36 points of the original image within that cell.

Since the attitude of the satellite affects the scan direction, the scan in general in neither perpendicular to the orbit, nor symmetric relative to the nadir. Moreover, the variable yaw causes the scan lines to be non-parallel.

Hence the image must be rectified. We desire an image with lines perpendicular to the satellite orbit and columns parallel to it. A transformation is created from the raw image to the warped image. Each pixel of the raw image is located by its ground X_e, Y_e coordinates using the technique above. Then its line and column number in the rectified image are calculated via the closest neighbor method.

The method of closest neighbor employs the distance of a warped pixel to the closest grid point. The intensity of a rectified grid point is the intensity of the original pixel with minimum distance to that point. The distance d is given by

$$d = \sqrt{\Delta k^2 + \Delta l^2}$$

where Δk and Δl are the differences between warped column and line and nearest grid column and line respectively.

Figure 8 shows a distance image produced by WARPM procedure. Increasing distance is marked by an increased blackening of the image.

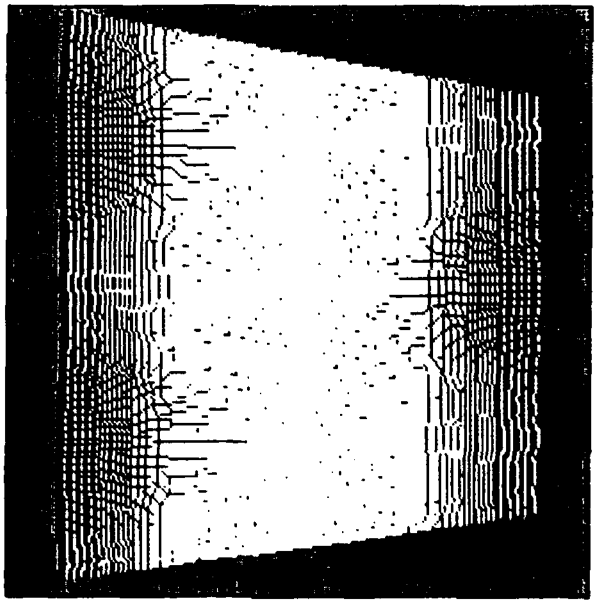

Figure .8: Distance image - scene 59 (file r8705212).

If the entire set of raw pixels is to fall within the borders of the warped image, an appropriate scale must be found for the new map. The chosen size of the warped image is $4800\,km \times 4800\,km$. Consequently, some edge pixels within the rectified image have no inverse transformation to the raw image, and are thus null. The empty border regions are marked by the grey tone in Figure 8.

The transformation from the raw image to the rectified image gives us an opportunity to change the way the spherical earth is projected onto the two dimensional image. The imaging method employed by the satellite creates a space oblique mercator projection of the ionospheric north pole region. The transformation of the raw pixels using a fixed absolute distance ($\frac{4800}{240} = 20\,\frac{km}{pixel}$) creates a polar stereographic projection.

.4 Photometric Processing

.4.1 Motivation

The photometric processing enhances the image in order to make use of the full dynamic range afforded by the image processing hardware. In a subsequent development, we devised a novel approach toward the separation of dayglow from aurora. The technique is based on a spatially variable intensity criteria. The dayglow intensity in every single image is fitted by a general function. Variables of this function are the solar senith angle, and the path length of the emitting layer. Pixels with an intensity larger than that function are defined as auroral ones.

.4.2 Geophysical Parameters

Four geophysical variables are computed:

- Inverse path length.
- Corrected $\cos\chi$.
- Number of hours since sunrise or sunset.
- Total daily solar exposure time.

These 4 geophysical parameters are stored in a single binary image 240×240 pixels large. It may be displayed as an ordinary image, where each parameter occupies an area of $120\,lines \times 120\,columns \times 1\,byte$. Figure 9 shows this image for scene 06 (file s87023f2). Inverse path length is on the upper-right, $cos\chi$ on the upper-left, daily solar time on the lower-right, and time since sunrise/sunset on the lower-left side of the image.

The path length D of the emitting layer as observed by the detector for a specific scan angle α is given by $D = p_{h_1} - p_{h_2}$, where p_{h_1} and p_{h_2} are the lengths of the vector $\vec{p}$ as it crosses the emitting later at heights h_1 and h_2

respectively. Since $\Delta h \ll R_{\oplus}$, D can be approximated by

$$\frac{D}{\Delta h} = \frac{(R_{\oplus} + h)}{\sqrt{(R_{\oplus} + H_s)^2 \cdot \cos^2 \alpha' - (R_{\oplus} + H_s)^2 + (R_{\oplus} + h)^2}}$$

The solar senith angle χ depends on the declination of the sun δ, the hour angle t of the sun, and the geographic latitude ϕ :

$$\cos \chi = \sin \delta \cdot \sin \phi + \cos \delta \cdot \cos \phi \cdot \cos t$$

The sun's declination angle is given by $sin \delta = \sin \epsilon \cdot \sin l$, where $\epsilon \simeq 23.5°$ is the inclination of the ecliptic to the equator, and l the celestial longitude of the sun, i.e. the longitude of the sun on the ecliptic relative to the equinox.

The amount of solar radiation hitting the atmosphere affects the airglow intensity. However, the functional dependence of $\cos \chi$ is incorrect at high solar senith angles due to the general failure of the plane-parallel approximation at these angles ([1]). By high solar senith angles we mean $90° + \psi \geq \chi \geq 65°$, where ψ is the 150 km UV sunset/sunrise dip angle. We correct $\cos \chi$ using modified Chapman function $Ch(\chi, X)$ values with a scale height gradient of $\frac{dH(O)}{dz} = 0.75$ at 150 km. $X = \frac{R_{\oplus} + h}{H(O)} = 170$, where $H(O) = 38.4\,km$ is the atomic oxygen scale height at 150 km ([21], and [23]). Following Kasachevskaya et al. ([10]), we assume $\psi_{sunrise} = 10°$, and $\psi_{sunset} = 5°$.

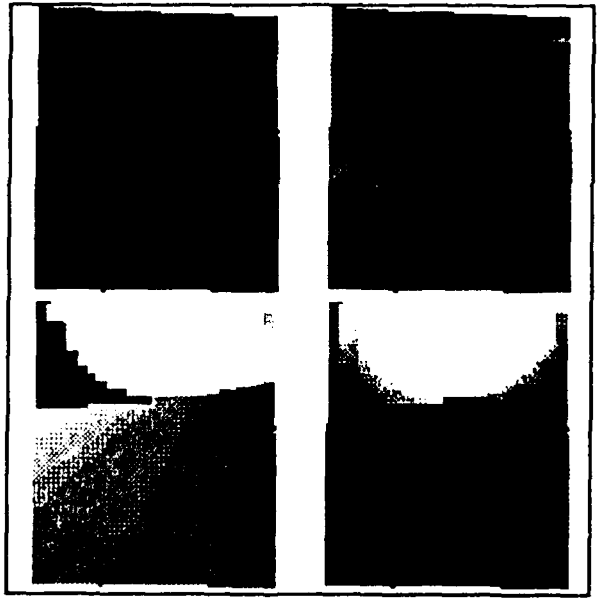

Figure .9: Four geophysical parameters - sel06.i

Figure 10 shows the difference between $Ch(\chi, X)$ and $\cos\chi$ as a function of solar zenith angle for $100° \geq \chi \geq 65°$. At $\chi = 65°$ there is a 5% difference between the values of the two functions. Thus we interpolate between these two functions in the range $70° \geq \chi \geq 65°$ to assure continuity.

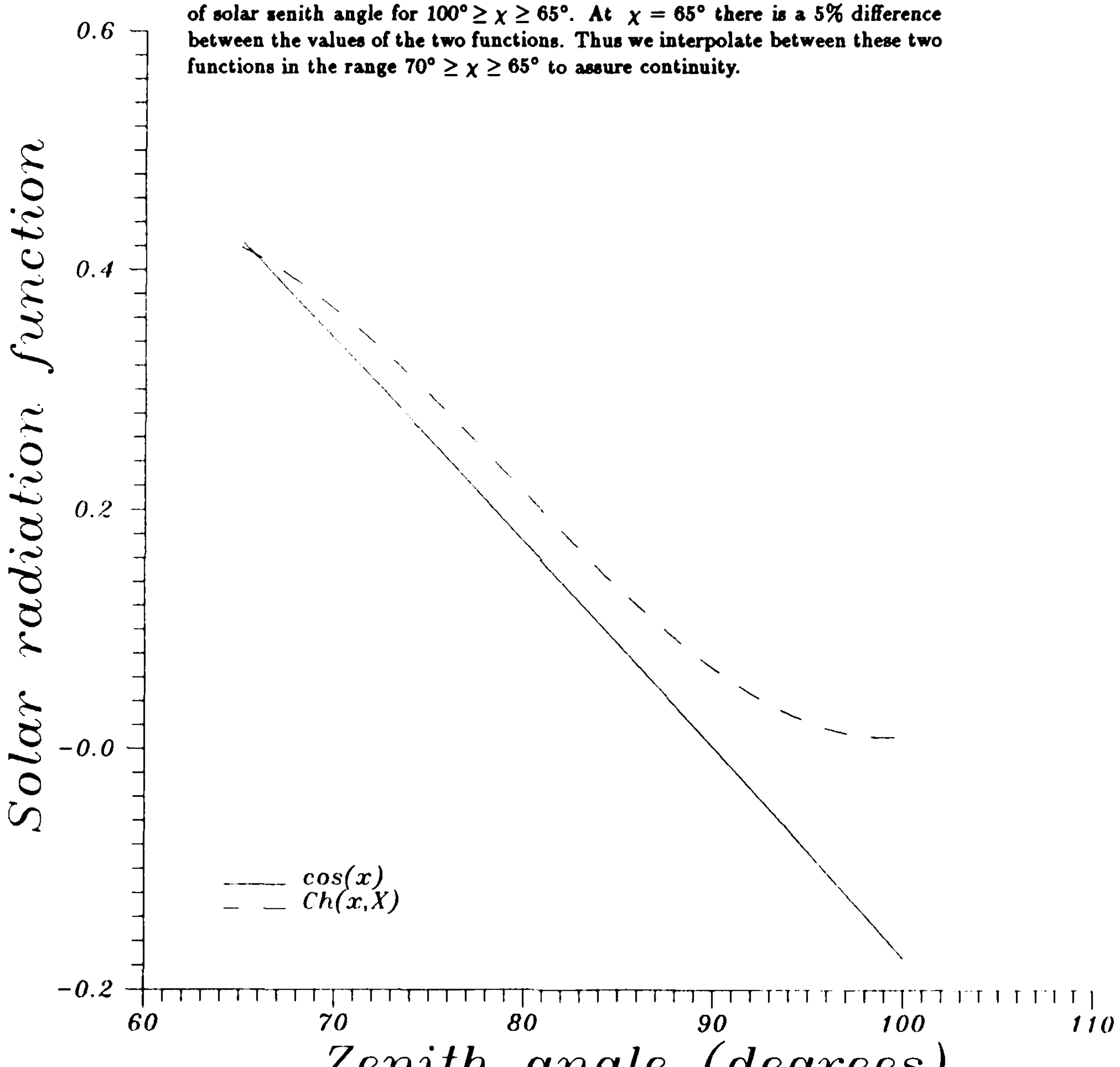

Figure .10: A comparison of $Ch(\chi, X)$ and $\cos\chi$ for $100° \geq \chi \geq 65°$.

.4.3 Enhancement and Filtering

As evident from Figure 4, the dynamic range of the raw image is rather poor. Detector 2 ($\lambda = 1596\AA$) has a dynamic range of ~ 50, whereas the dynamic range of detector 1 ($\lambda = 1356\AA$) is ~ 5. In order to utilise the full dynamic range afforded by the image processing hardware (255), a stretching routine is applied to the image. The amplification factor m is based on the particular image statistics. It is set to $m = 255/b_{99.9}$, where $b_{99.9}$ is the brightness of the 99.9 percentile in the cumulative histogram of the raw image.

Since the signal to noise ratio of the image is limited by count statistic ($\frac{signal}{noise} = \frac{1}{\sqrt{signal}}$), the low signal implies a relatively high noise level. The effect of non-discriminate linear amplification on noisy pixels is highly unwelcome. Hence a smoothing routine is applied to the amplified image. We use the most-frequent value filter in order to eliminate single noise pixels.

If the image features some airglow background, it may be desired to subtract it. The subject of background subtraction will be discussed in the following subsection. However, the background airglow must be smoothed before trying to fit any continuous function to it. Thus we apply two averaging filters to the image before initiating the background subtraction: an auroral , and an airglow averaging filter. The auroral filter has the dimensions of $5\,columns \times 3\,lines$; the airglow filter is $15\,columns \times 7\,lines$ large. We have chosen the ratio of filter width by height to be ~ 2 to approximately compensate for the angular ratio of the distance between resampled pixels ($1.3°/0.56°$).

.4.4 Background Subtraction

The night glow intensity is below the detection threshold of the two working detectors (1, and 2). Therefore when one discusses airglow subtraction in Polar BEAR images, one actually refers to dayglow and twilight glow only.

Airglow in general is defined in a negative sense. It is the entire atmospheric radiation excluding aurora, Rayleigh scattering, and thermal emission. The sole source of airglow energy is solar radiation. Dayglow consists of prompt radiation, and night glow of delayed emission. Twilight glow is dayglow observed from the night sky. Thus the transmission of twilight glow differs from the transmission of dayglow through the atmosphere.

However, not enough twilight glow pixels are present in a typical image to warrant a statistically valid fit. Hence a single function is fitted to the two airglow domains. Our aim here is to fit an analytic function of geophysical parameters to the geometrically corrected image in order to separate aurora from airglow.

A least-squares fit is performed on the brightness b of a pixel as a function of two variables: path length l, and the Chapman function s (corrected $\cos(\chi)$).

The fit of the function

$$b = c_0 \cdot p^{c_p} \cdot s^{c_s}$$

produces three coefficients: c_0, c_p, and c_s.

Results of such fits to 9 scenes and 2 detectors are presented in Table 6. $\hat{c}_0$ is the average brightness (c_0) normalised to unit path length ($l = 1$) and sero senith distance ($s = 1$). σ_0 is the standard deviation around the mean of $\log_{10} b$, where b is the original pixel brightness. σ_f is the standard deviation around the mean of the expression $\log_{10} b - c_p \cdot \log_{10} l - c_s \cdot \log_{10} s$. Ratios $\frac{\sigma_f}{\sigma_0} < 1$ indicate the successfulness of the fit.

scene	detector 1					detector 2				
#	$\hat{c}_0$	c_p	c_s	σ_0	σ_f	$\hat{c}_0$	c_p	c_s	σ_0	σ_f
06	100.4	0.70	1.08	0.18	0.11	89.8	0.77	0.84	0.16	0.03
07	111.6	0.69	1.02	0.15	0.08	221.9	0.67	1.19	0.13	0.04
34	81.0	0.70	0.98	0.19	0.10	77.5	0.82	1.03	0.19	0.04
35	45.7	0.76	0.60	0.19	0.11	64.3	0.83	0.88	0.18	0.05
37	87.5	0.60	0.90	0.18	0.11	63.9	0.84	0.82	0.19	0.06
38	68.5	0.58	0.43	0.17	0.12	66.8	0.84	0.75	0.19	0.07
40	26.0	1.10	0.46	0.23	0.08	62.6	0.88	0.87	0.20	0.03
57	39.6	0.90	0.47	0.20	0.10	57.4	0.94	0.79	0.22	0.04
59	45.8	0.62	0.70	0.14	0.06	103.2	0.69	1.12	0.18	0.04

Table .6: Least-squares fit to airglow intensities.

Program GEOMLSQ uses the coefficients found to subtract the expected from the actual brightness of every pixel. Following this subtraction, if the brightness of a pixel is larger than the amplification factor m, then it is an auroral one. A subsidiary criteria of an auroral brightness threshold is used in conjunction with the above subtraction in order to distinguish airglow from auroral pixels.

The program uses the warped image and the geophysical parameters to create an auroral image. An image that compares the fitted intensity values with the actual ones is also provided.

Once a purely auroral image has been formed, the raw image is rewarped in order to produce a non-averaged auroral image. Program REWARP re-warps the raw image while checking the auroral image as produced by GEOMLSQ. Non-auroral pixels are set to a signal of 1 (pixels in the warped image that carry a sero brightness are pixels outside the imaging field-of-view).

Figure 11 shows the same image shown in Figure 4 photometrically and geometrically processed. Most of the noise has been smoothed out, and the majority of airglow background subtracted.

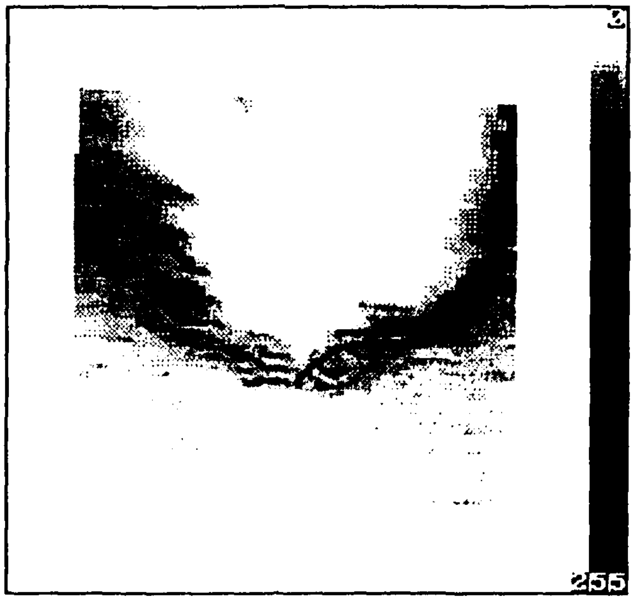

Figure .11: Auroral image - scene 07, $\lambda = 1356$Å.

.5 Geometric Error Analysis

The major purpose of the geometric processing is to map the image correctly on the geographic coordinate system. The location of each pixel is a function of the satellite attitude parameters and the height of the emitting layer. The accuracy of the mapping depends on the accuracy of these parameters.

We have analysed the effect of the main uncertainties, i.e. satellite attitude angles and height of emitting layer, on the geographic location of pixels as a function of scan angle.

The accuracy of the control system is specified as 1°. However, our roll correction technique implies an error of 1–2° for the roll angle, and by implication for the pitch and yaw angles as well. We have assumed a constant height of $150\,km$ for the emitting layer, and believe its accuracy to be $\sim 50\,km$.

A statistically random approach has been chosen for the error analysis. A large number of iterations were run to compute the geographic location of pixels for normally random distributions of the above variables. The result was a distribution of the mapped location, for which the average and standard deviations were computed.

The standard deviation from the exact location (zero errors in variables) is given by an angle whose apex is at the center of the earth. One may assume, then, that the maximum error in either latitude or longitude (geographic or geomagnetic) is this angle.

Let P be the pitch angle, R the roll angle, and Y - the yaw angle. $<P>$, $<R>$, and $<Y>$ are the average values, and σ_P, σ_R, and σ_Y the standard deviations of these angles respectively. We used these six values plus the height of the emitting layer ($H = 150 \pm 50\,km$) to create random groups of these variables normally distributed around the mean. We chose $<P> = 1.7°, <R> = -1.0°$, and $<Y> = 7°$. The standard deviations are $\sigma_P = \sigma_Y = 1$–$2°$, with the exception of $\sigma_R = 1°$ due to the roll correction.

The simulation was run for seven scan angles: $0°, 30°, 40°, 50°, 55°, 60°$, and $62°$ for three cases :

- Error in attitude angles only.
- Error in emitting layer height only.
- Error in both attitude angles and emitting layer height.

Table 7 shows the results of these error simulation runs. Each case was iterated 5000 times to create a the statistic of a normal distribution. To test the randomness of the procedure, the average values and standard deviations of the distributions of attitude angles were compared to the corresponding input values. $\hat{\delta}$ is the average value of the error; σ_δ - the standard deviation of the error (in degrees).

σ_P	σ_R	σ_Y	σ_H		scan angle						
					0	30	40	50	55	60	62
1.0	1.0	1.5	0	$\hat{\delta}$	0.2	0.2	0.3	0.4	0.6	1.2	1.8
				σ_δ	0.1	0.1	0.1	0.2	0.4	0.9	1.3
1.0	1.0	1.0	50	$\hat{\delta}$	0.2	0.3	0.5	0.7	1.0	1.8	2.4
				σ_δ	0.1	0.2	0.3	0.5	0.7	1.4	1.6
2.0	1.0	2.0	0	$\hat{\delta}$	0.3	0.3	0.4	0.5	0.7	1.3	2.0
				σ_δ	0.1	0.2	0.2	0.3	0.4	0.9	1.3
0.0	0.0	0.0	50	$\hat{\delta}$	0.0	0.2	0.4	0.6	0.8	1.4	2.1
				σ_δ	0.0	0.2	0.3	0.4	0.6	1.1	1.5
2.0	1.0	2.0	50	$\hat{\delta}$	0.3	0.4	0.5	0.8	1.1	2.0	2.5
				σ_δ	0.1	0.2	0.3	0.5	0.7	1.5	1.6

Table .7: Angular error in pixel ground location.

The error increases with scan angle. It is larger than 1° for scan angles ≥60°. In the worst case, an average error of 2° exists for a pixel located at a scan angle of 60°.

The results of the error simulations also point to a practical aspect. We can give an upper limit of 1° on the error anywhere in the image if we limit the mapping to scan angles relative to satellite nadir that are less than 55 degrees. An error of 1° is quite acceptable, since it is also the accuracy of the corrected geomagnetic coordinate system ([9]), and the accuracy of Feldstein's oval ([22]), to be discussed in the following section.

Thus a calculation of a lower-limit scan angle derived from an angle of 55° relative to the nadir is performed by program SCENE. In the course of pixel projection to its ground location, procedure WARPM utilises this limit to avoid mapping pixels beyond the corresponding scan angle. The price paid is loss of a small part of the original image coverage, and converting linear image edges to edges that follow the satellite roll.

We compare the mapping of an image without and with the above procedure in the following two Figures. Figure 12 shows an auroral map in which all possible scan angles are used. Figure 13 depicts the same scene (scene 44 - file s8705312) where the mapping has been limited to scan angles that correspond to angles ≤ 55° relative to the nadir.

Figure .12: Mapping of an image without a 55° nadir angle limit.

Figure .13: Mapping of an image with a 55° nadir angle limit.

.6 Coordinate Systems

.6.1 Geographic System

Two programs are available for overlaying a geographic grid upon an image: LANDMASS and GMCOORD. LANDMASS plots a geographic grid and/or landmass features upon the warped image. GMCOORD plots a geographic grid upon the image with a somewhat better accuracy than LANDMASS.

A note should be made regarding the landmass feature of the first program. The pixels of the warped image are mapped onto a sphere 150 kilometers above ground, whereas landmasses are on the ground earth. The image and landmasses are thus projected to a common picture from a view point of satellite nadir at image central line.

Program TERMINATOR marks the sun terminator on a 240x240 image mapped by cartesian geographic coordinates. A user may choose the solar dip angle of the terminator. The default value is set to the 150 kilometers sunset solar dip angle $(-12.3°)$.

Figure 14 shows scene 06 (file s87023f2) for which no airglow has been subtracted. A geographic grid has been overlaid by GMCOORD and landmass features were drawn by LANDMASS. Two terminators are marked: the geometric horison at solar senith angle $\chi = 90°$, and the $150\,km$ sunset/sunrise terminator at $\chi = 102.3°$.

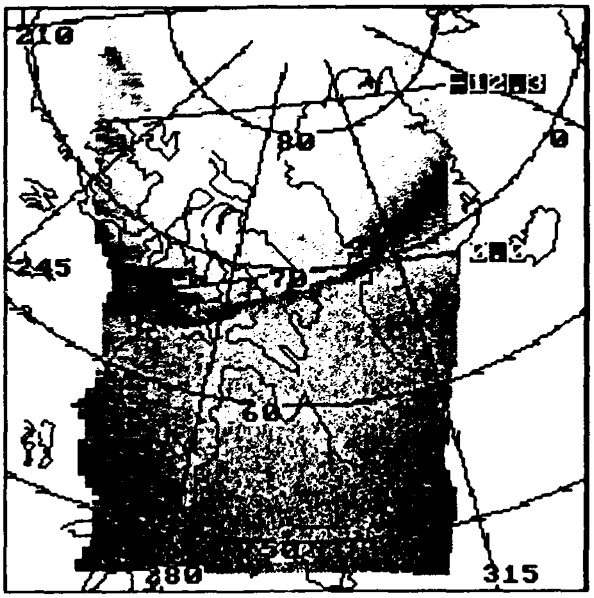

Figure .14: Image 062 with a geographic grid, landmasses, and terminators.

.6.2 Geomagnetic System

Two different techniques are available for geomagnetic coordinate system application. GMCOORD, as in the geographic case, plots a geomagnetic grid upon the image. AURPLOT does exactly the opposite - it warps the image onto a fixed coordinate system. Both allow the use of two different coordinate systems: magnetic dipole, and corrected geomagnetic.

The magnetic dipole is a first approximation to the geomagnetic field. The imaginary dipole is located at the center of the earth, and inclined by 11.5° relative to earth's rotation axis. The dipole crosses the earth's surface at 78.5°N, 291.0°E, which is the north pole of the geomagnetic dipole system.

The field lines are given by $r = r_0 \cdot \sin^2\theta$; r_0 is the geocentric distance where the field line crosses the magnetic equator.

Note that the dipole system is simply a spherical system similar to the geographic system. Thus any point on the earth with geographic coordinates ϕ, λ is translated to the geomagnetic dipole system by rotating the system around the geographic axis by 291 degrees and around the new axis by 11.5 degrees.

The coordinate system most used in the literature is the corrected geomagnetic system. Hakura ([7]) computed the ground shift of the magnetic field lines due to the first four terms in the spherical harmonic development of the potential following the dipole term. Hakura's system was improved by Gustafsson ([6]), who included two more harmonic terms. Gustafsson showed that the maximum contribution of these terms is 130 kilometers, to which the 7–th term contributed less than 30 km.

The corrected system is computed by following a common point on the equator along a dipole field line, and along a corrected field line (with the higher terms) to the ground. The ground distance on the sphere is then the correction to the dipole system for that specific point.

Gustafsson created a table to convert geographic coordinates to corrected geomagnetic coordinates by using the first seven harmonic terms. The table supplies corrected geomagnetic coordinates for every 2° of geographic latitude, and every 5° of geographic longitude. Intermediate points are calculated by interpolation.

The corrected system of Gustafsson is a ground system, whereas the aurora occurs at an altitude of ~150 kilometers. A dipole correction to the corrected geomagnetic latitude Θ_c as a function of height h is given by

$$\cos^2\Theta_c(h) = \frac{R_\oplus + h}{R_\oplus} \cdot \cos^2\Theta_c(0)$$

where $R_\oplus$ is earth's radius.

The warping of an image to a fixed geomagnetic polar stereographic system leaves 'holes', similar to the ones created when magnifying an image. These holes are filled by a median filter.

The approach of projecting an image to a fixed coordinate system affords us to view and compare all the images on a common ground. Furthermore, multiple-image operations are readily available.

Figure 15 shows two images taken during a single pass over the north pole by two different receiving stations. Image 402 (file r87051k2) and 412 (file t87051k2) are rotated to align local magnetic noon at the top of the map. Corrected magnetic latitude lines are marked at 10° intervals; magnetic local time at 6 hours intervals.

The two images span a total integration time of 22 minutes, of which 2 minutes are overlapping time. The 102.3° terminator of this overlapping time is the arc at the central part of the map. Background airglow has been subtracted. The sigsag border is the overall field-of-view of the two images. The limit to scan angle of 55° relative to satellite nadir has been applied.

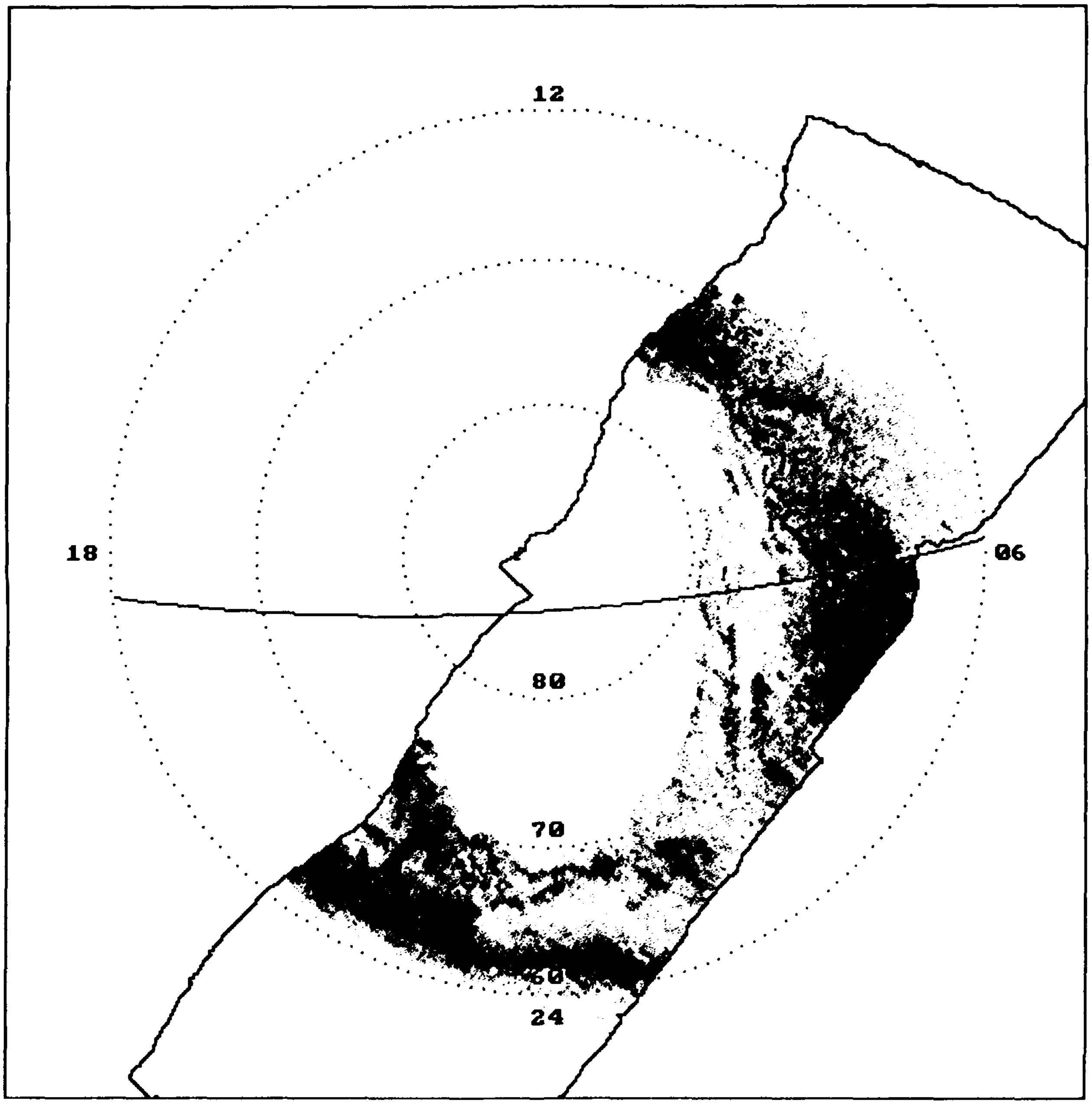

Figure .15: Images 402 and 412 on a corrected magnetic time-latitude system.

.7 Results and Conclusions

.7.1 Multiple Auroral Image Averaging

Feldstein et al. ([3], and [4]) prepared ovals of auroral activity as a function of the geomagnetic Q index. Feldstein's ovals are the results of optical images obtained by all sky cameras on the ground. Within the oval boundaries there is a chance of 70% for the aurora to occur at any time. The boundaries are the results of averaging the poleward and equatorward boundaries of the aurora as detected by these cameras. The ovals represent mainly discrete aurora, since the continuous aurora exhibits a much lower contrast, and is much weaker in intensity per square sky degree than the discrete aurora.

The fixed coordinate system described in the previous section allows us to average many images, and create the VUV version of Feldstein's ovals. A major advantage this work has on Feldstein's is the fact that we can include daylight aurora. Also the relatively small bandwidth of the detector spectral sensitivity ($\sim 30Å$) implies we are looking mainly at a single species (OI).

Program AURMEAN combines auroral images to produce three maps - images coverage, normalised auroral frequency, and average intensity. Normalised frequency is the number of times aurora was present in a certain piece of sky relative to the total number of times that piece of sky was imaged.

We have processed 45 scenes at two wavelengths: 1596Å (detector 1), and 1356Å (detector 2). The images were grouped according to integer values of the K_p index, and the Q index. The binning was required in order to gather a reasonable number of images per group for averaging. Also Feldstein's ovals are grouped according to Q values, so K_p binning is a must for this kind of comparison. Images with K_p = 2+, 3, and 3-, for example, were binned under the $K_p = 3$ group.

K_p	Q	scene #
0	0	23 24 28 38
1	1	06 07 15 16 19 20 25 27 33 34 37 45 46 48
2	2	08 09 11 17 53 55
3	4	10 13 14 18 21 22 29 52 56 57
4	5	35 36 39 40 41 43 44 54 58 59
5	6	42

Table .8: Scene numbers according to K_p and Q values.

Table 8 lists all scenes that contributed to the VUV ovals. A single scene inhabits the $K_p = 5$ group, therefore ignored. Although the sise of the entire sample is reasonable, considering the amount of processing required, the sample per group is rather small. This effects both the degree to which the value is representative of the value of a large distribution of averaged images, and the total coverage of the images.

Figures 16–25 depict auroral frequency as a function of K_p. The local magnetic time - corrected geomagnetic latitude system is used. Borders describe the total field of view of the ensemble of images. Notice that in almost all cases the total coverage of the averaged images does not supply us with a full coverage of the upper part of the northern geomagnetic hemisphere.

Figures 26–35 depict average auroral intensity as a function of K_p. The same coordinate system is used. The ovals of Feldstein are present in Figures 16–35.

The conclusions to be drawn from the VUV ovals are as follows :

- The aurora in ultraviolet radiation appears in ovals that surround the geomagnetic pole; the center of the ovals is *not* at the pole.
- The latitude span of the aurora is greatest around local geomagnetic midnight; it is 4° at $K_p = 4$.
- As the magnetic activity rises (K_p increases), the poleward boundary of the aurora turns from an oval to a circle with a radius of $\sim 14°$ centered on the geomagnetic pole.
- In general there is a good correlation between the VUV ovals and Feldstein's oval; a conspicuous exception is the dayside aurora at low K_p; at $K_p = 0, 1$ the maximum latitude difference is 5°.

There are a few plausible explanations to the discrepancy between our maps and Feldstein's ovals at low K_p around local magnetic noon. Since the statistical coverage of the dayside is rather poor both in our study and in Feldstein's, it may simply be a statistical error. We intend to expand our processing in the future to include dozens of images in each map. Thus this point, at least regarding the statistical validity of our maps, will most certainly be cleared in the near future.

One major difference that exists between Feldstein's dayside aurora and this one is the fact that the first one covered only winter arcs at night, whereas our work includes daylight aurora that coexists with dayglow. Although background dayglow has been subtracted, the physics of the emitting species (e.g. density, height, etc.) and atmospheric transfer function may differ.

Also consider the situation of a temporally dynamic dayside aurora, even at low K_ps. Averaging two small samples of arcs may result in large differences in average location and intensity.

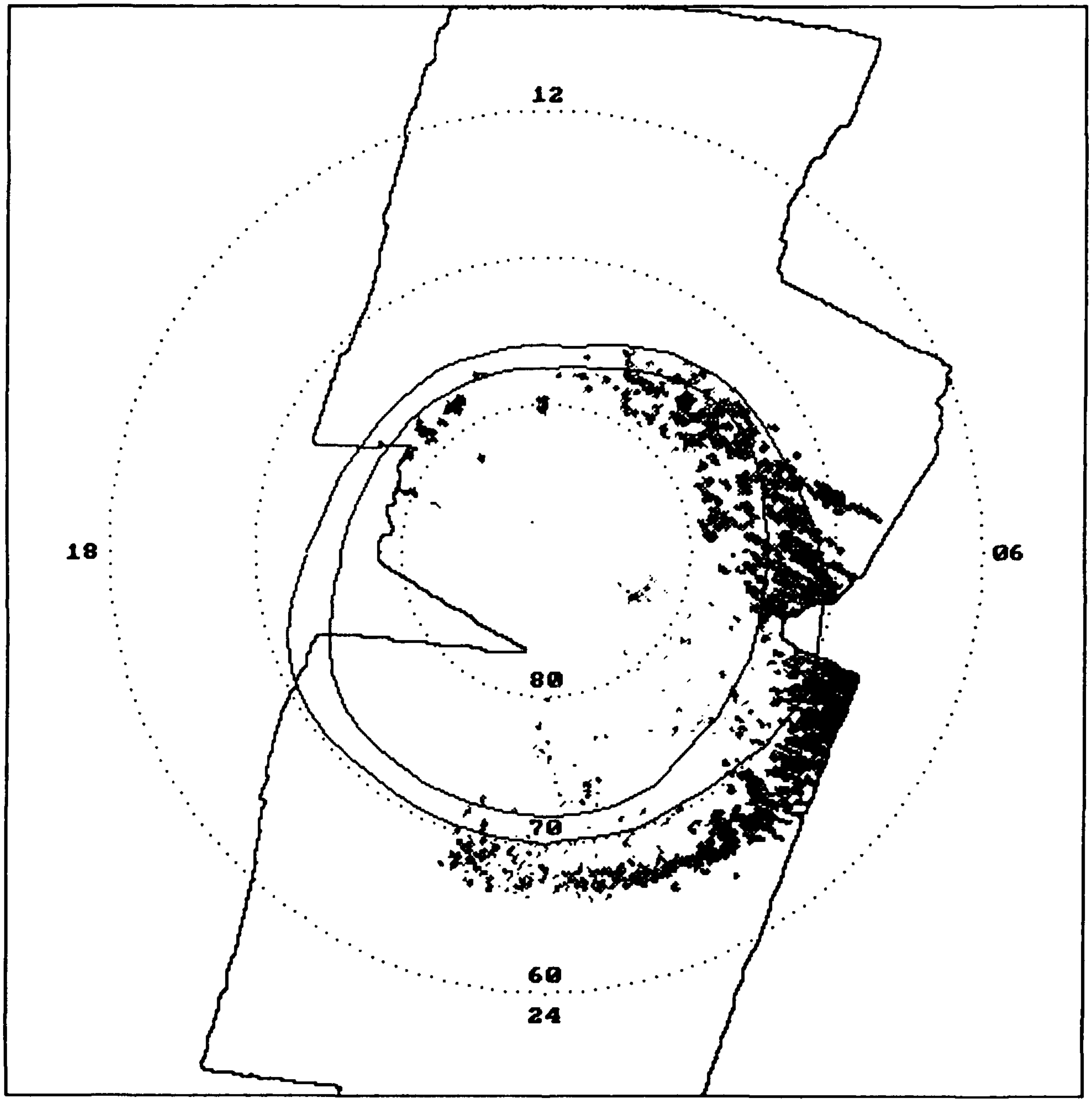

Figure .16: Auroral frequency - $K_p = 0$, $\lambda = 1596\AA$.

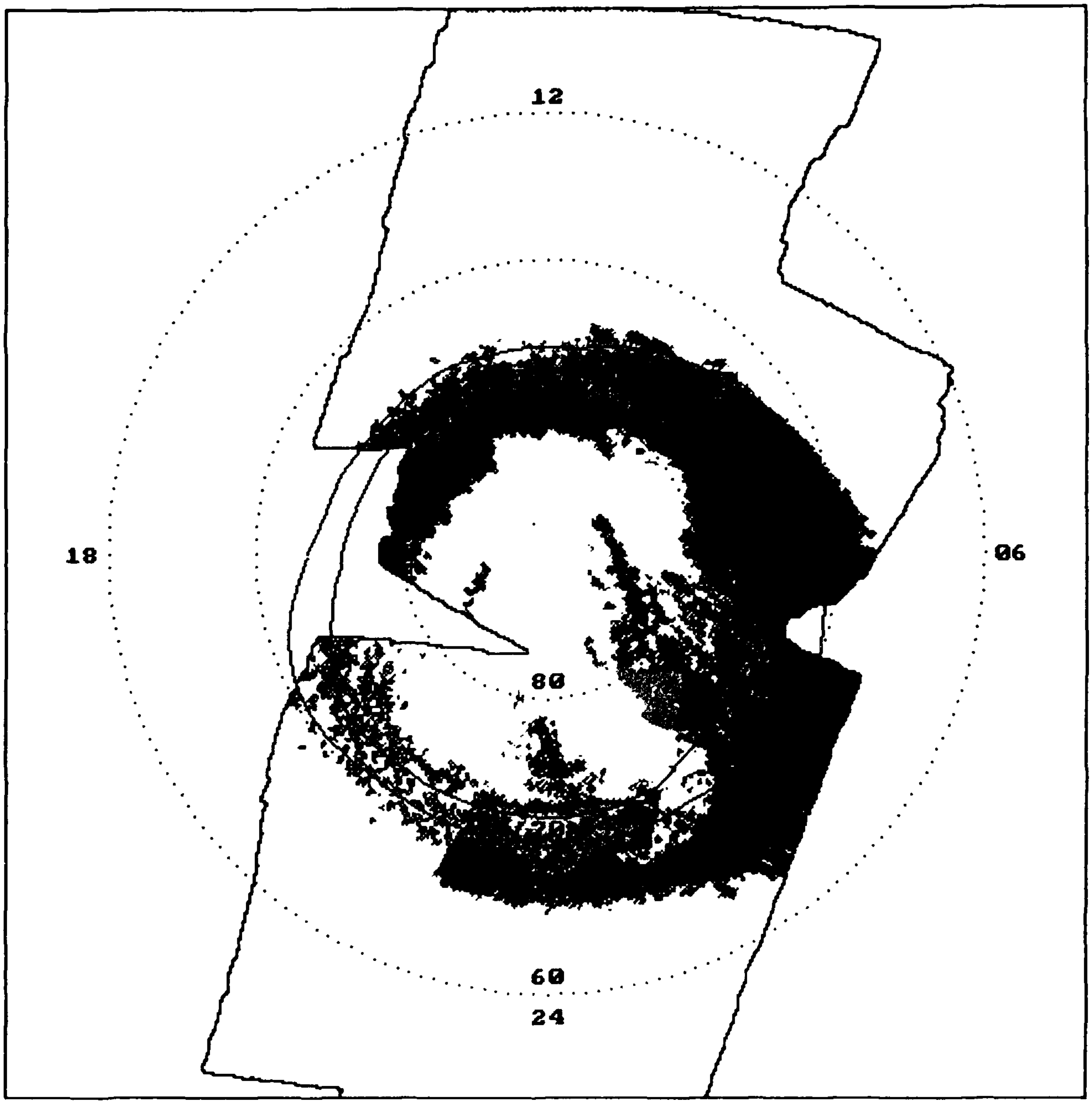

Figure .17: Auroral frequency - $K_p = 0$, $\lambda = 1356\AA$.

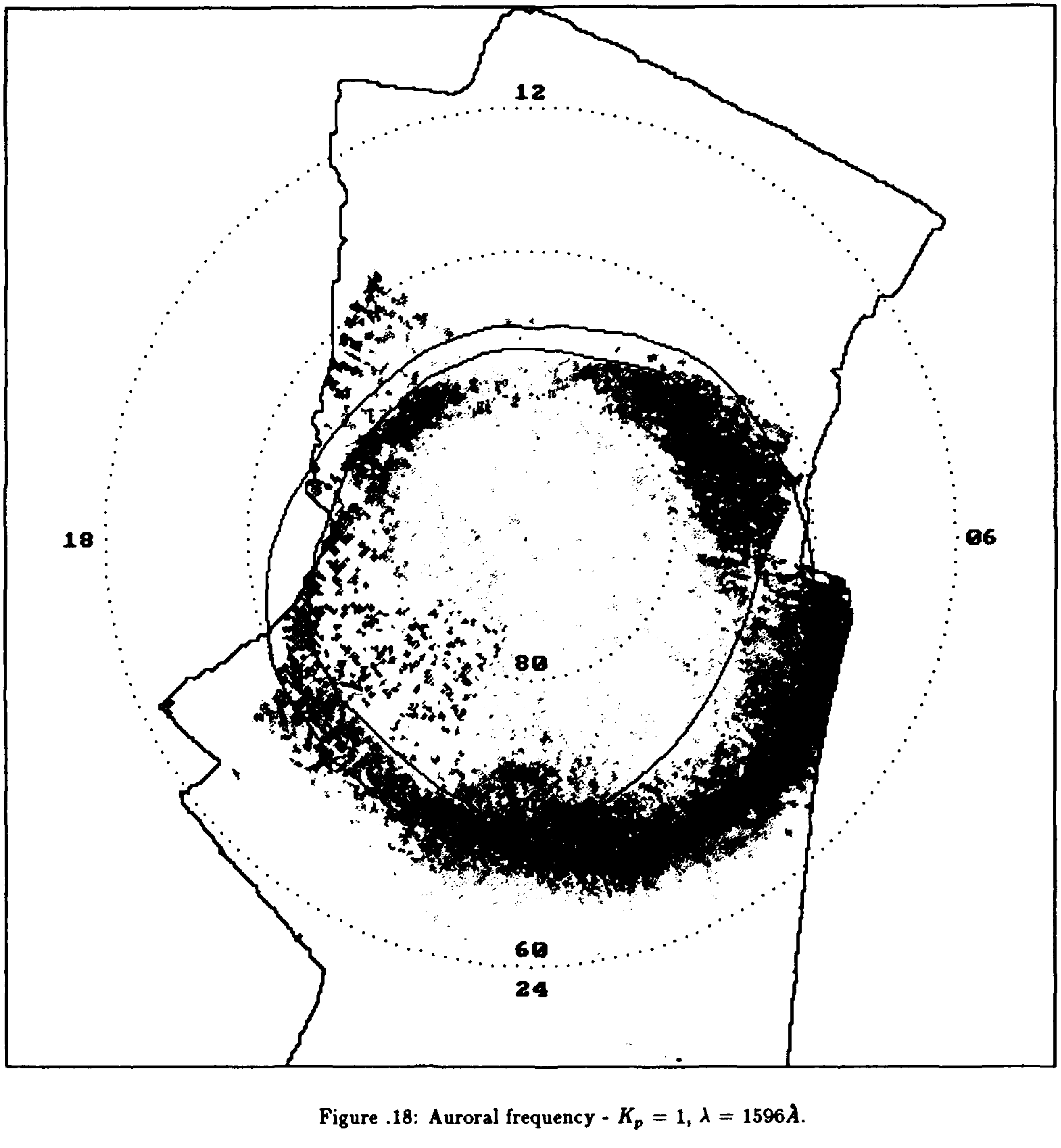

Figure .18: Auroral frequency - $K_p = 1$, $\lambda = 1596\AA$.

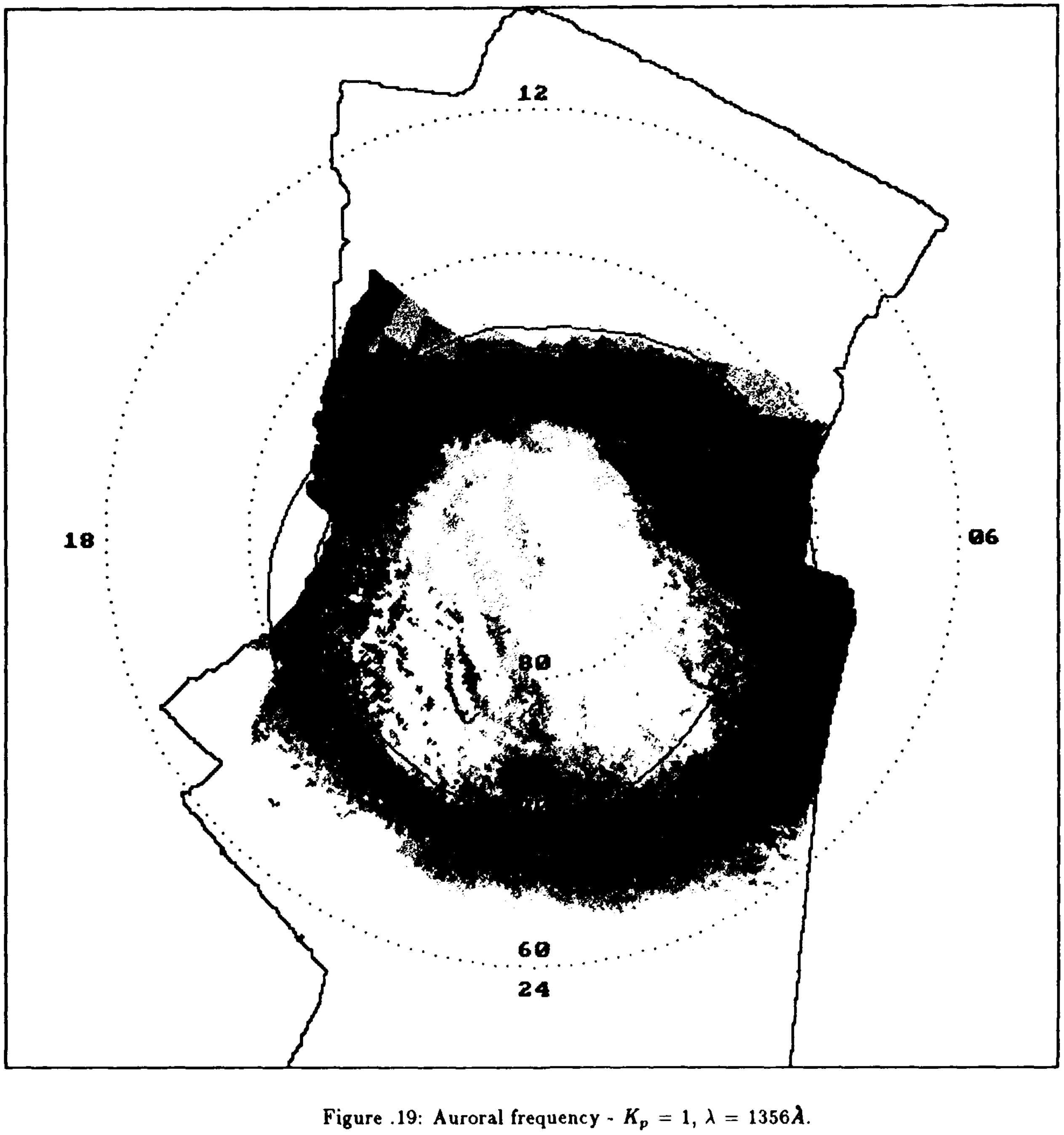

Figure .19: Auroral frequency - $K_p = 1$, $\lambda = 1356Å$.

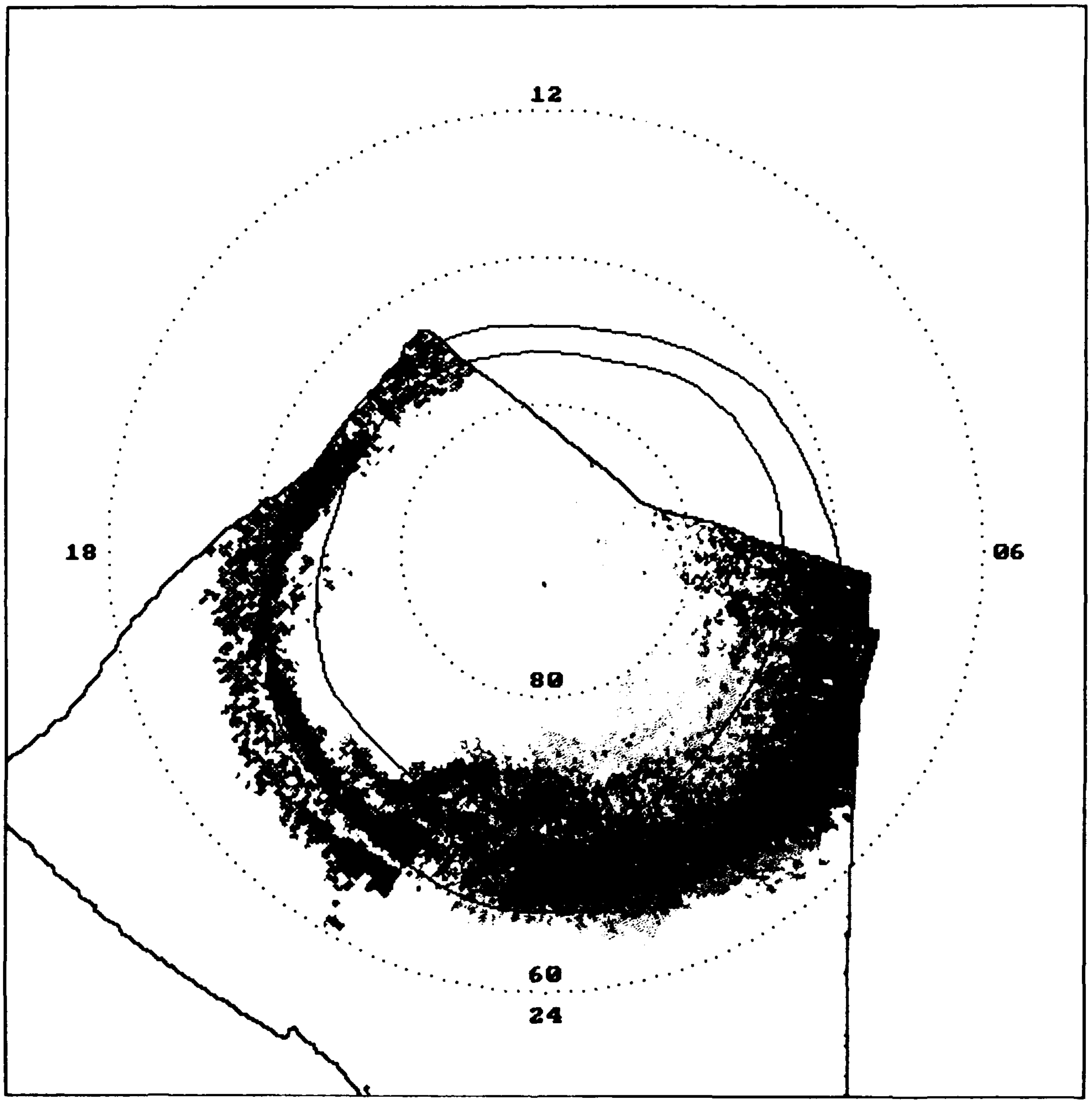

Figure .20: Auroral frequency - $K_p = 2$, $\lambda = 1596\AA$.

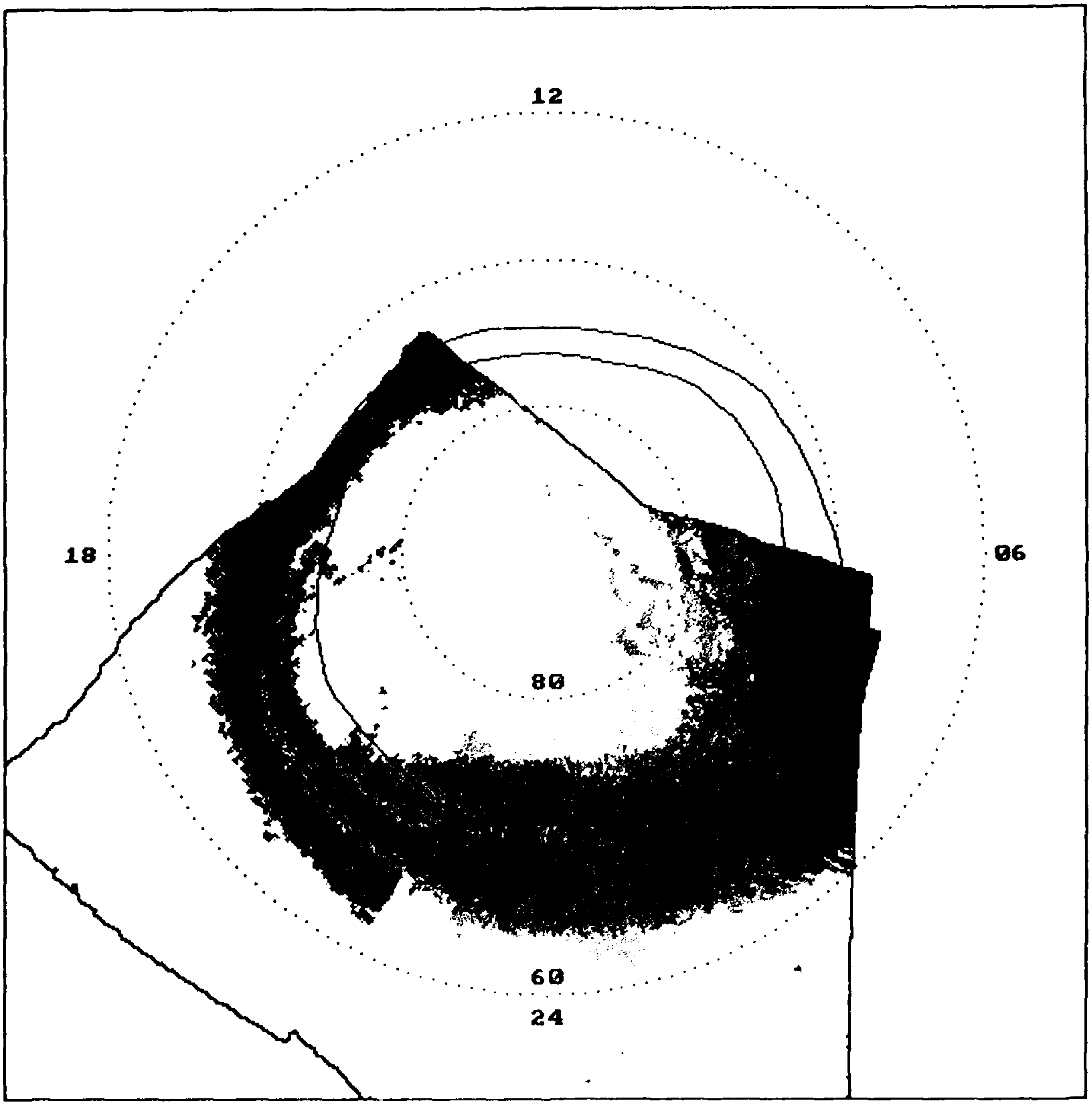

Figure .21: Auroral frequency - $K_p = 2$, $\lambda = 1356\AA$.

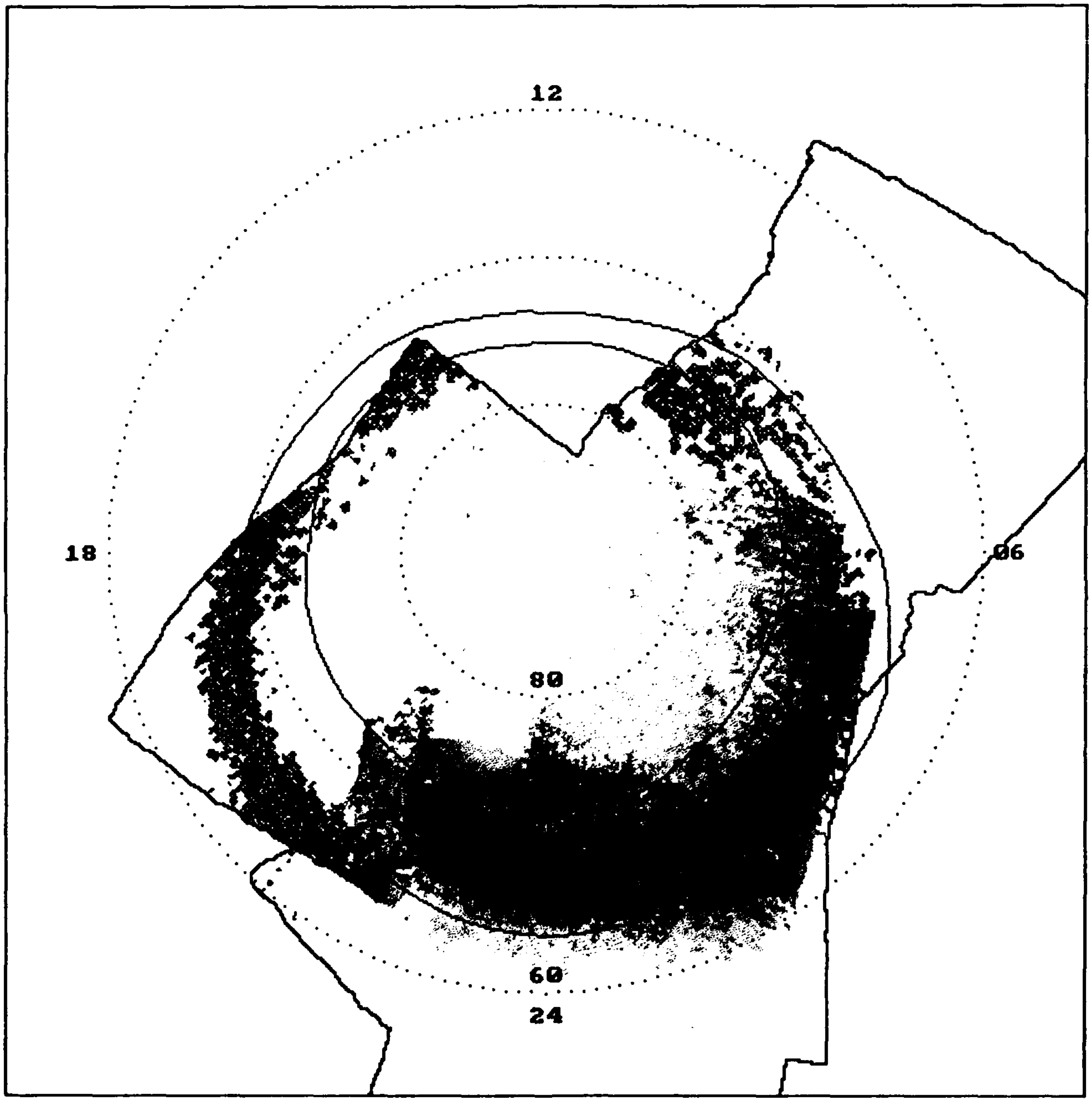

Figure .22: Auroral frequency - $K_p = 3$, $\lambda = 1596Å$.

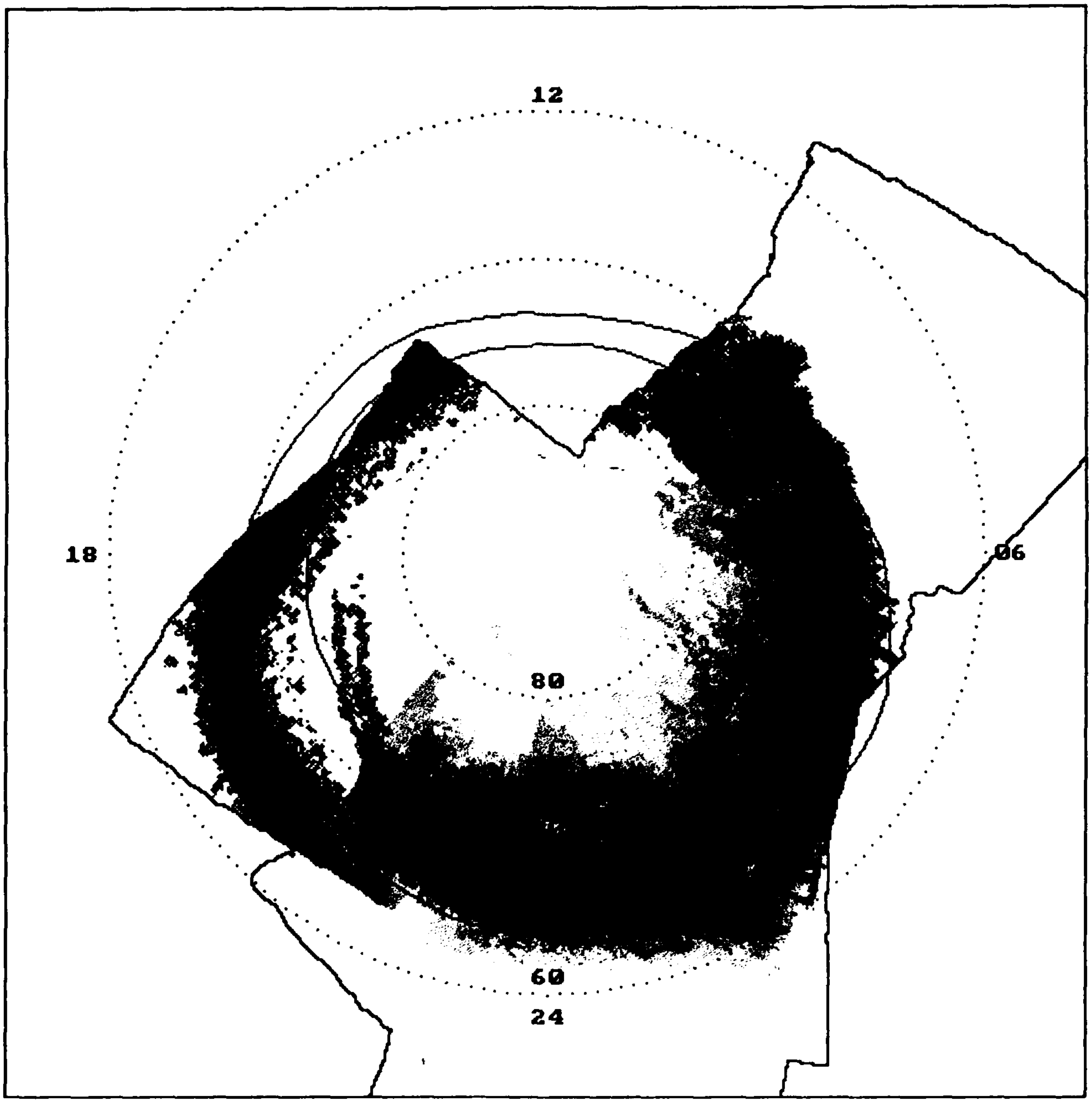

Figure .23: Auroral frequency - $K_p = 3$, $\lambda = 1356Å$.

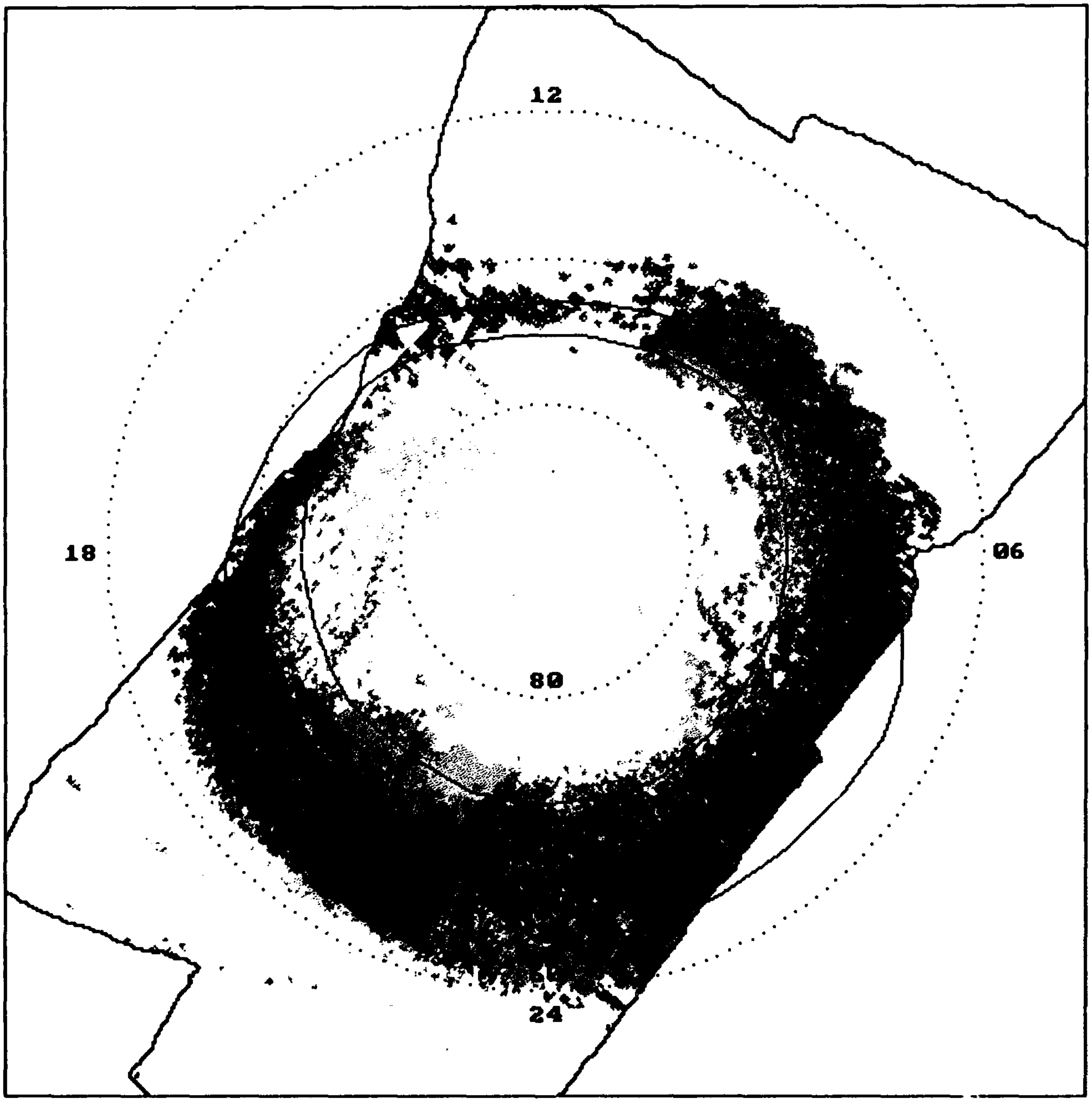

Figure .24: Auroral frequency - $K_p = 4$, $\lambda = 1596\AA$.

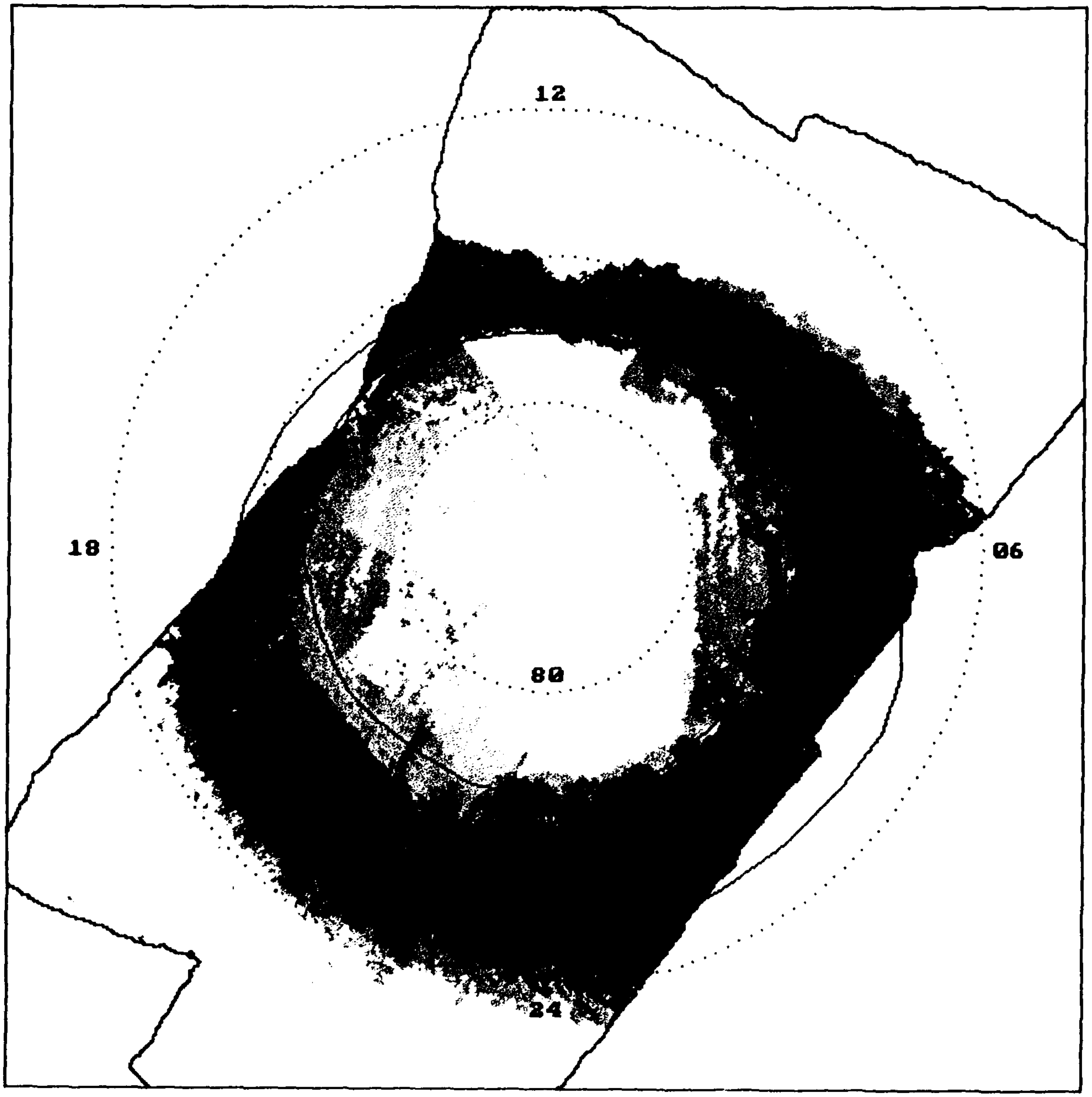

Figure .25: Auroral frequency - $K_p = 4$, $\lambda = 1356Å$.

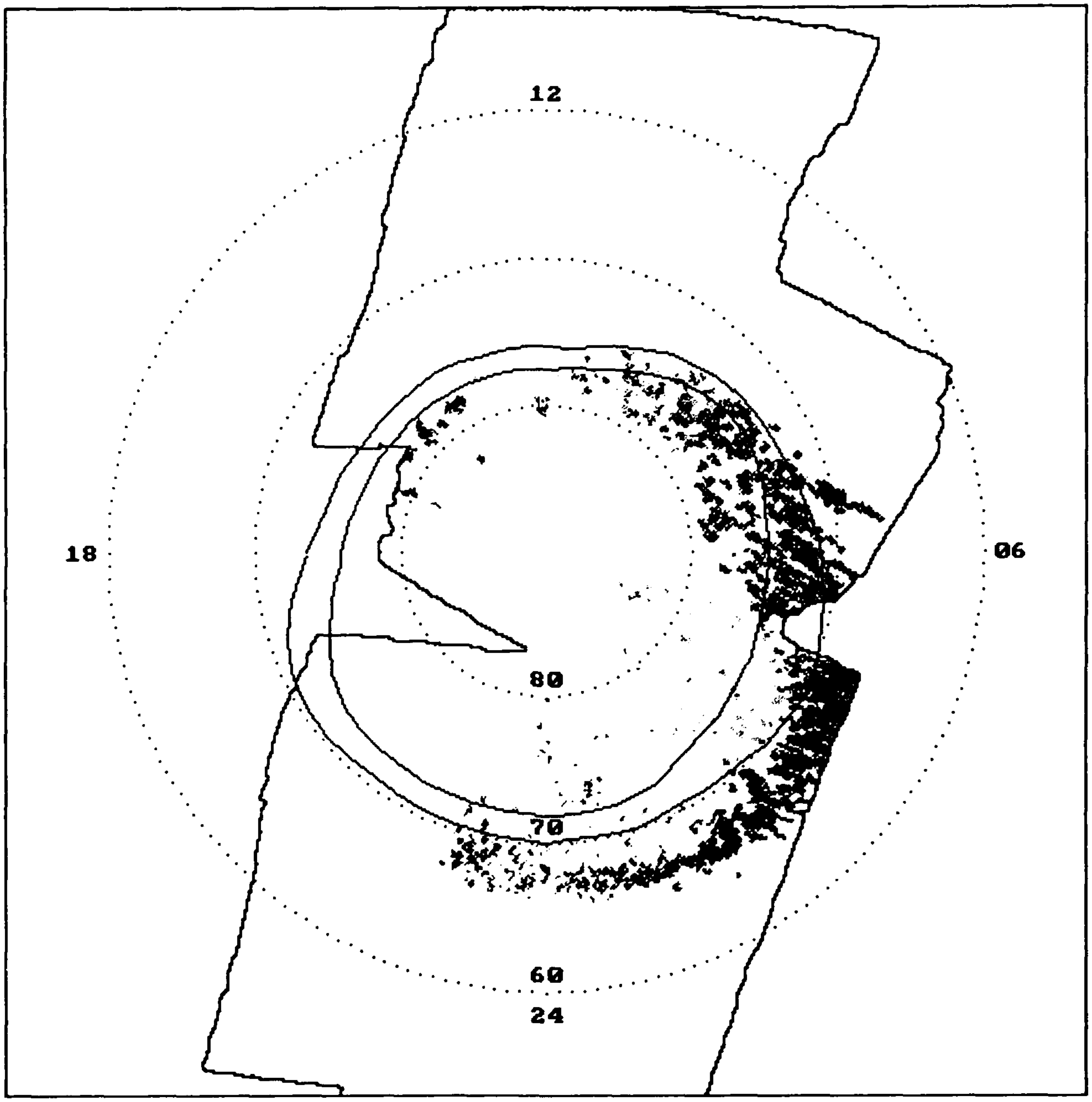

Figure .26: Average auroral intensity - $K_p = 0$, $\lambda = 1596Å$.

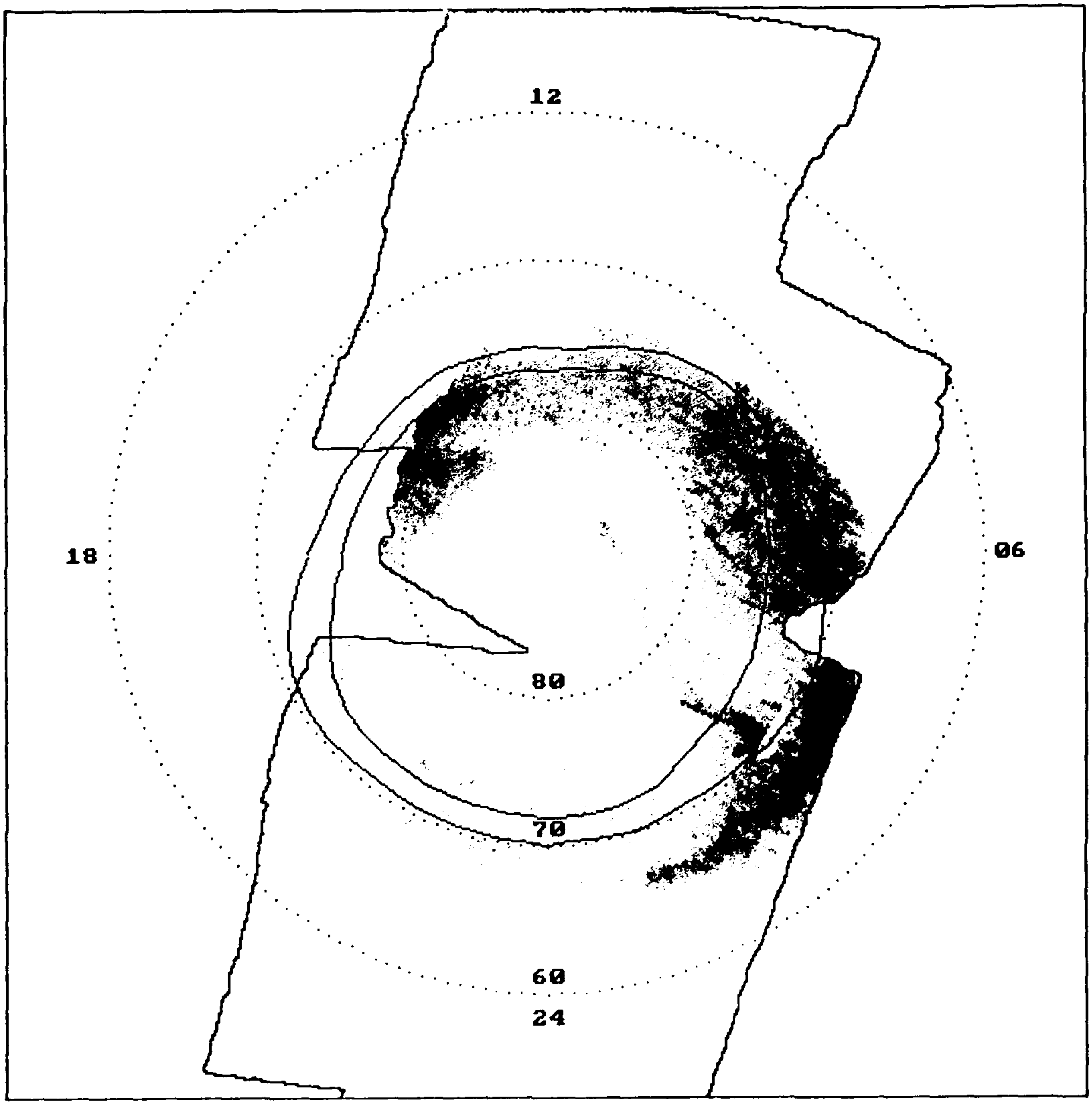

Figure .27: Average auroral intensity - $K_p = 0$, $\lambda = 1356Å$.

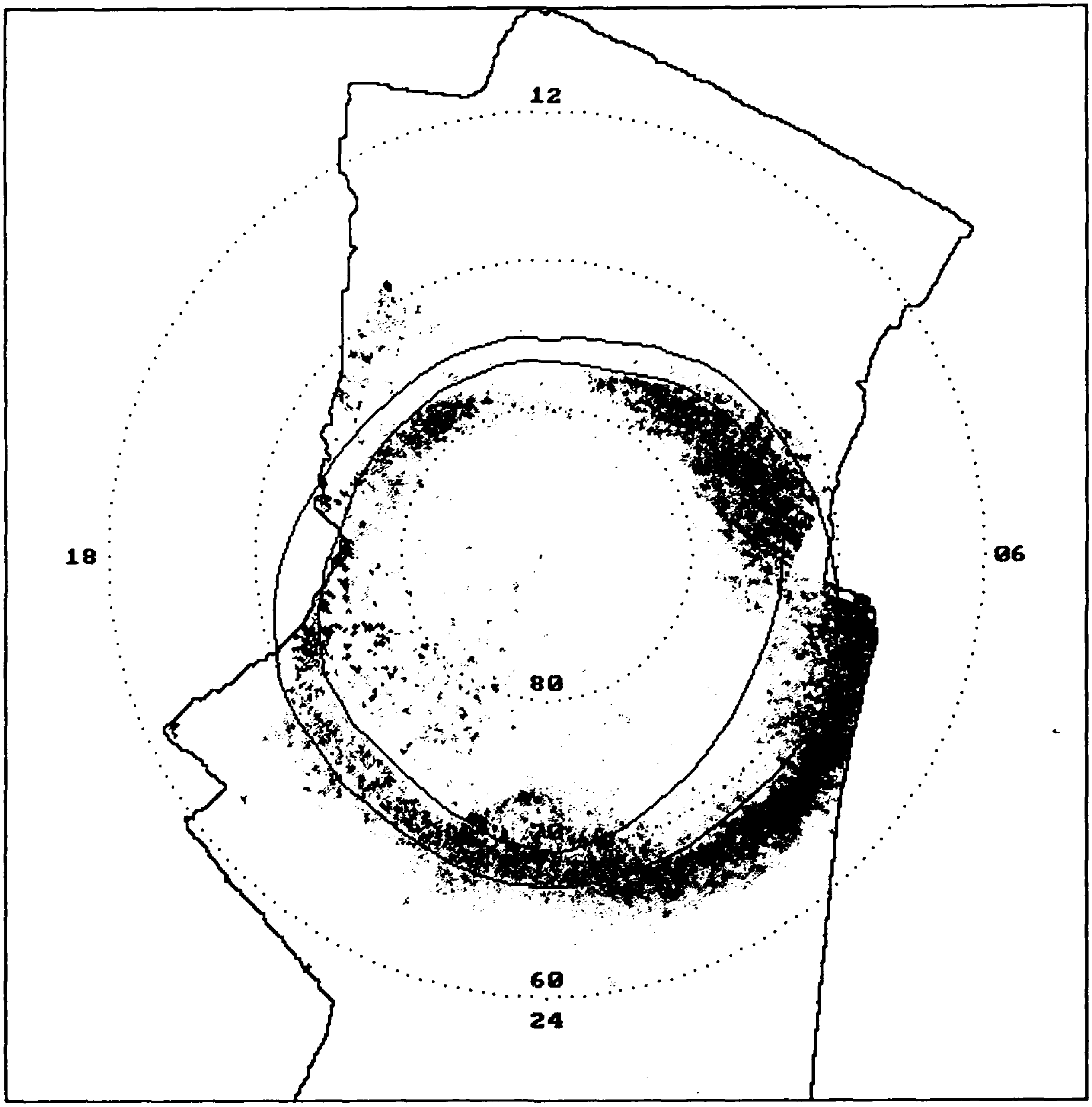

Figure .28: Average auroral intensity - $K_p = 1$, $\lambda = 1596\AA$.

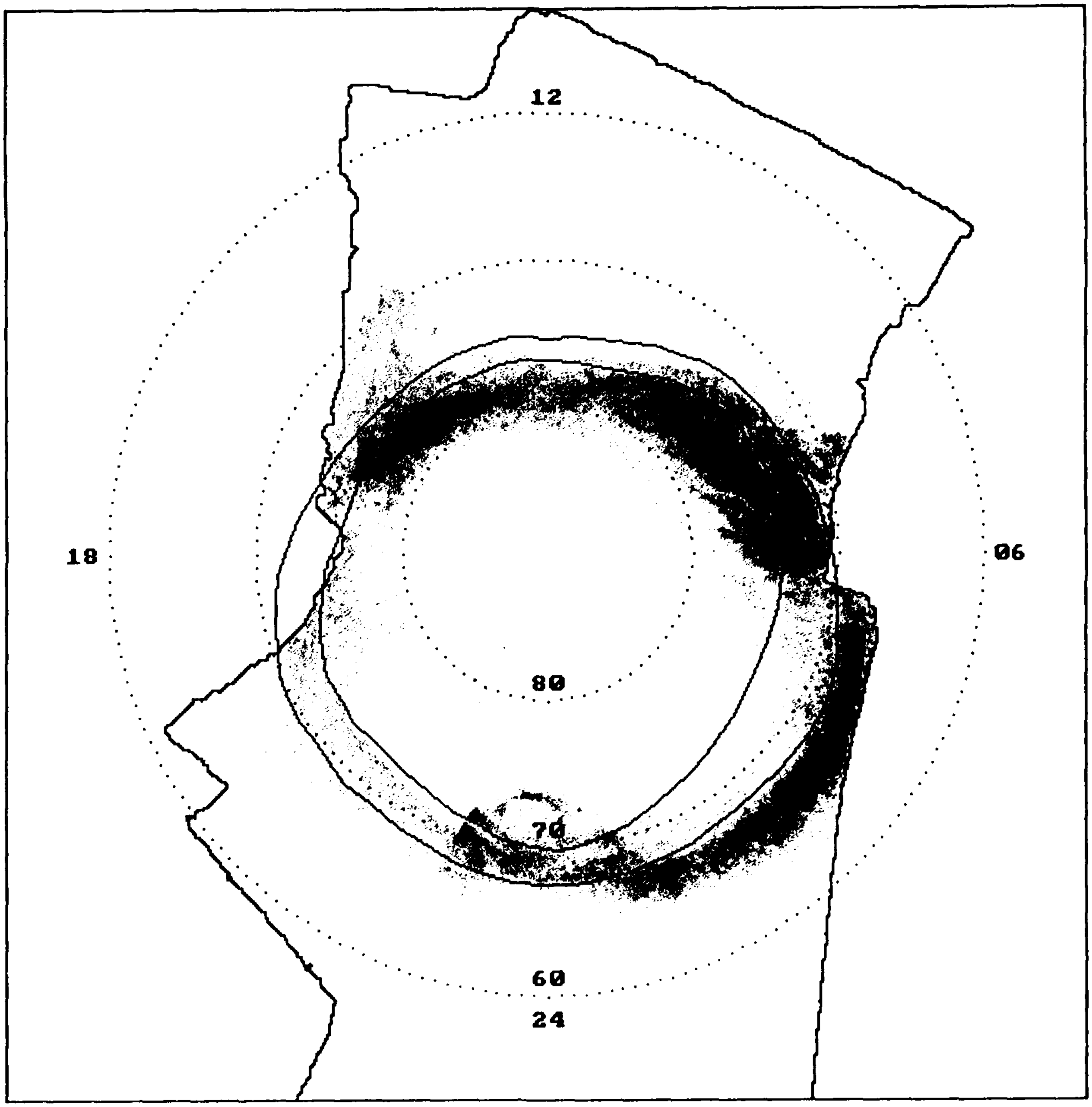

Figure .29: Average auroral intensity - $K_p = 1$, $\lambda = 1356Å$.

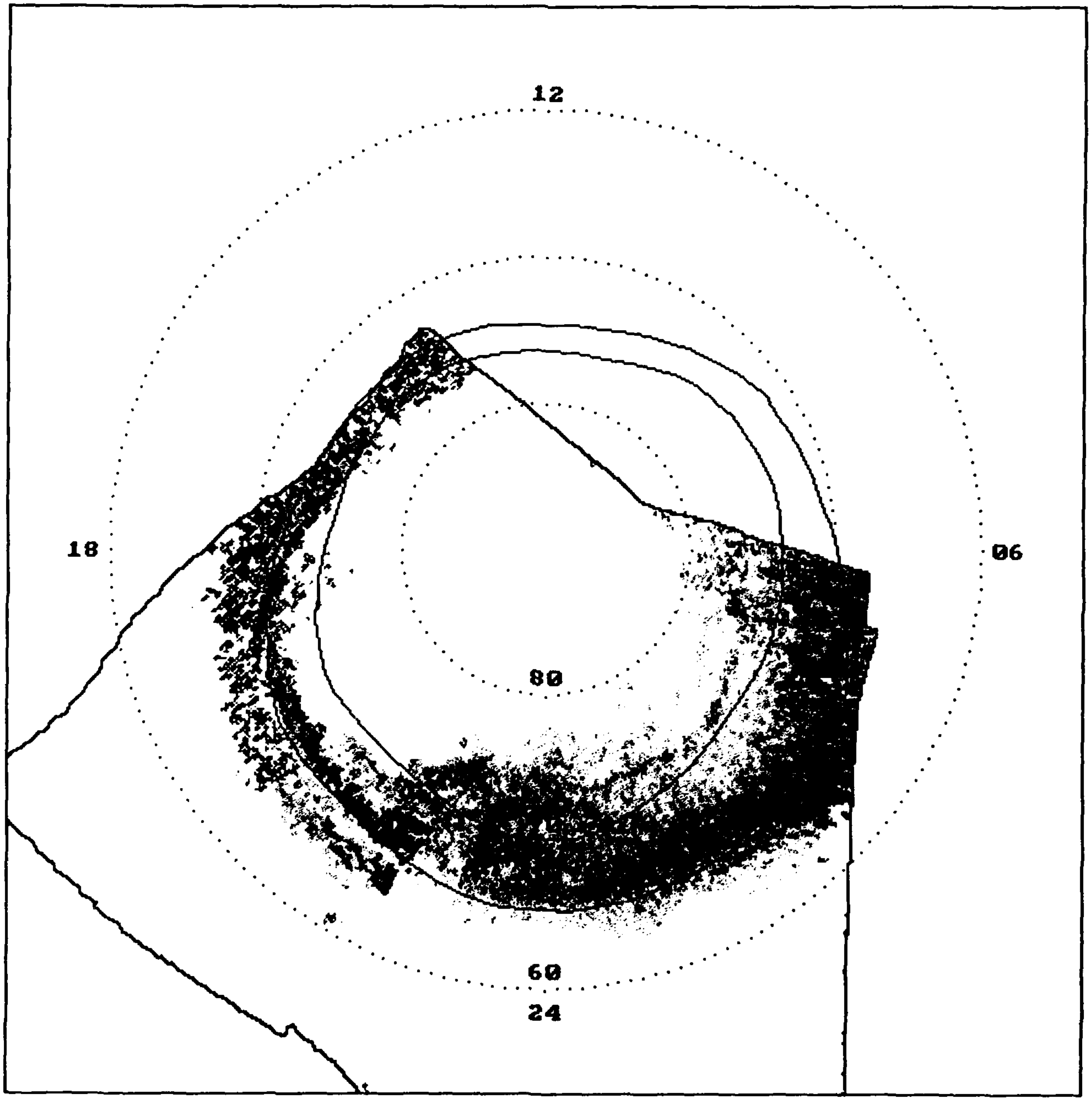

Figure .30: Average auroral intensity - $K_p = 2$, $\lambda = 1596\text{Å}$.

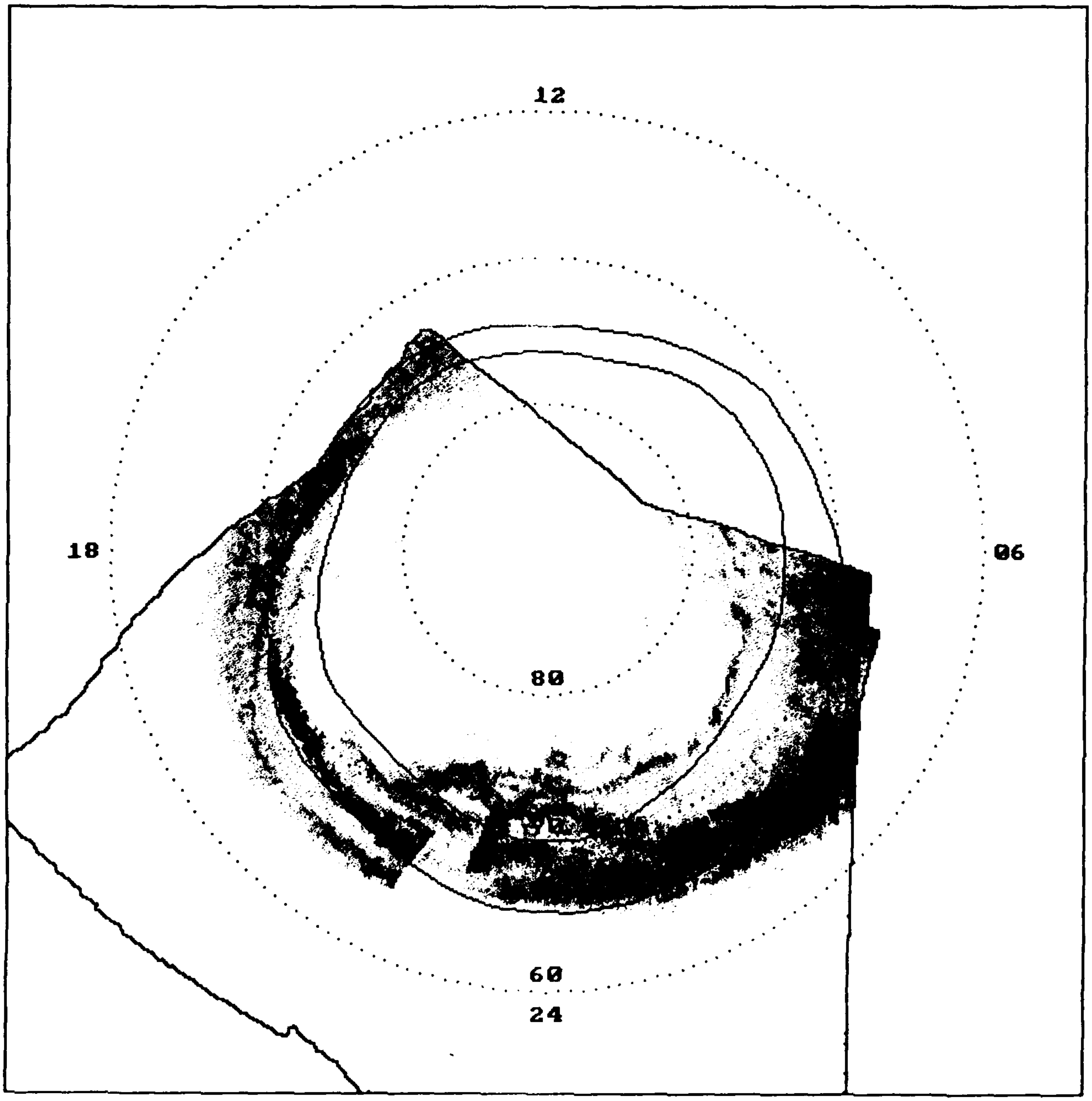

Figure .31: Average auroral intensity - $K_p = 2$, $\lambda = 1356\AA$.

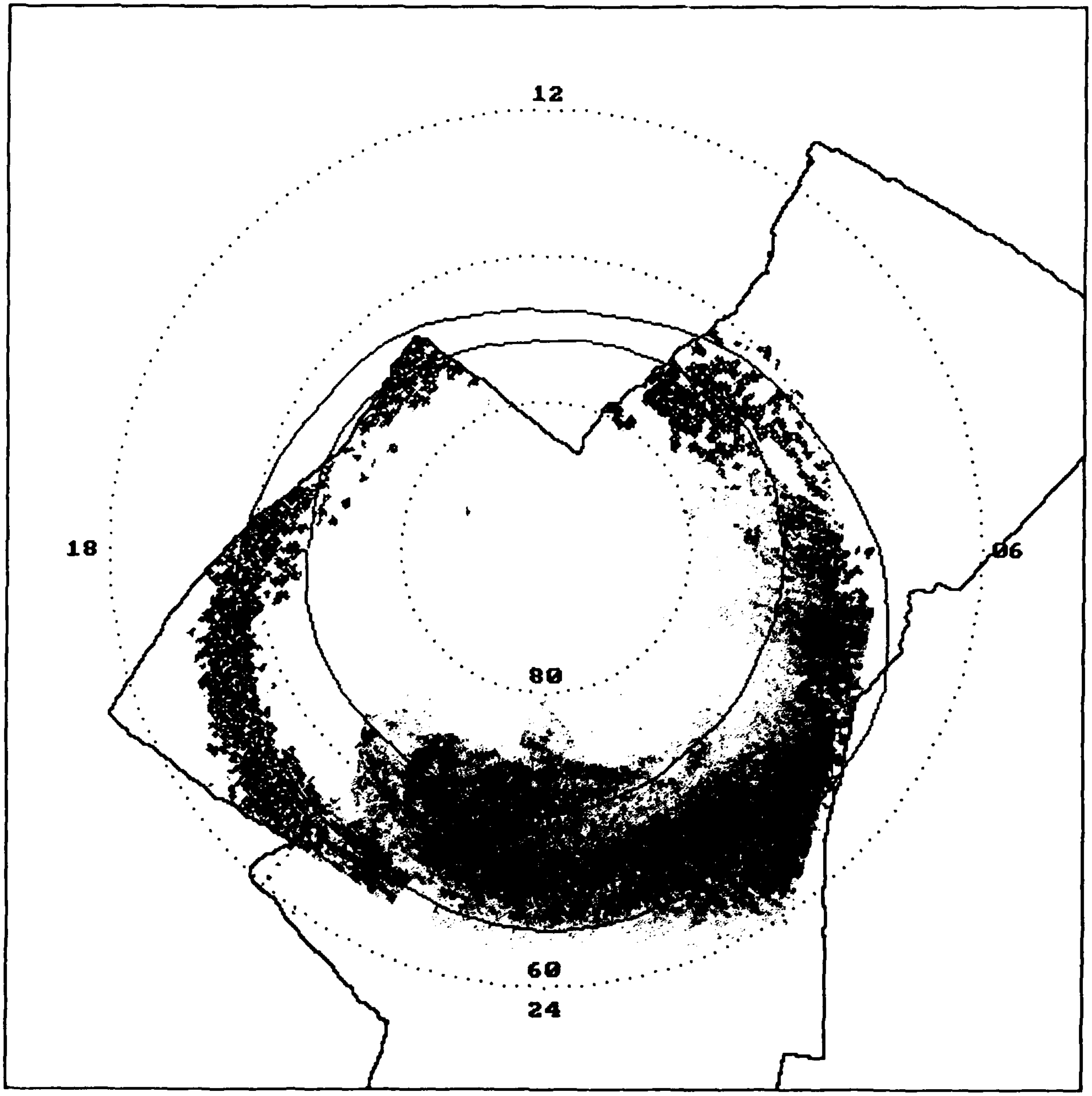

Figure .32: Average auroral intensity - $K_p = 3$, $\lambda = 1596Å$.

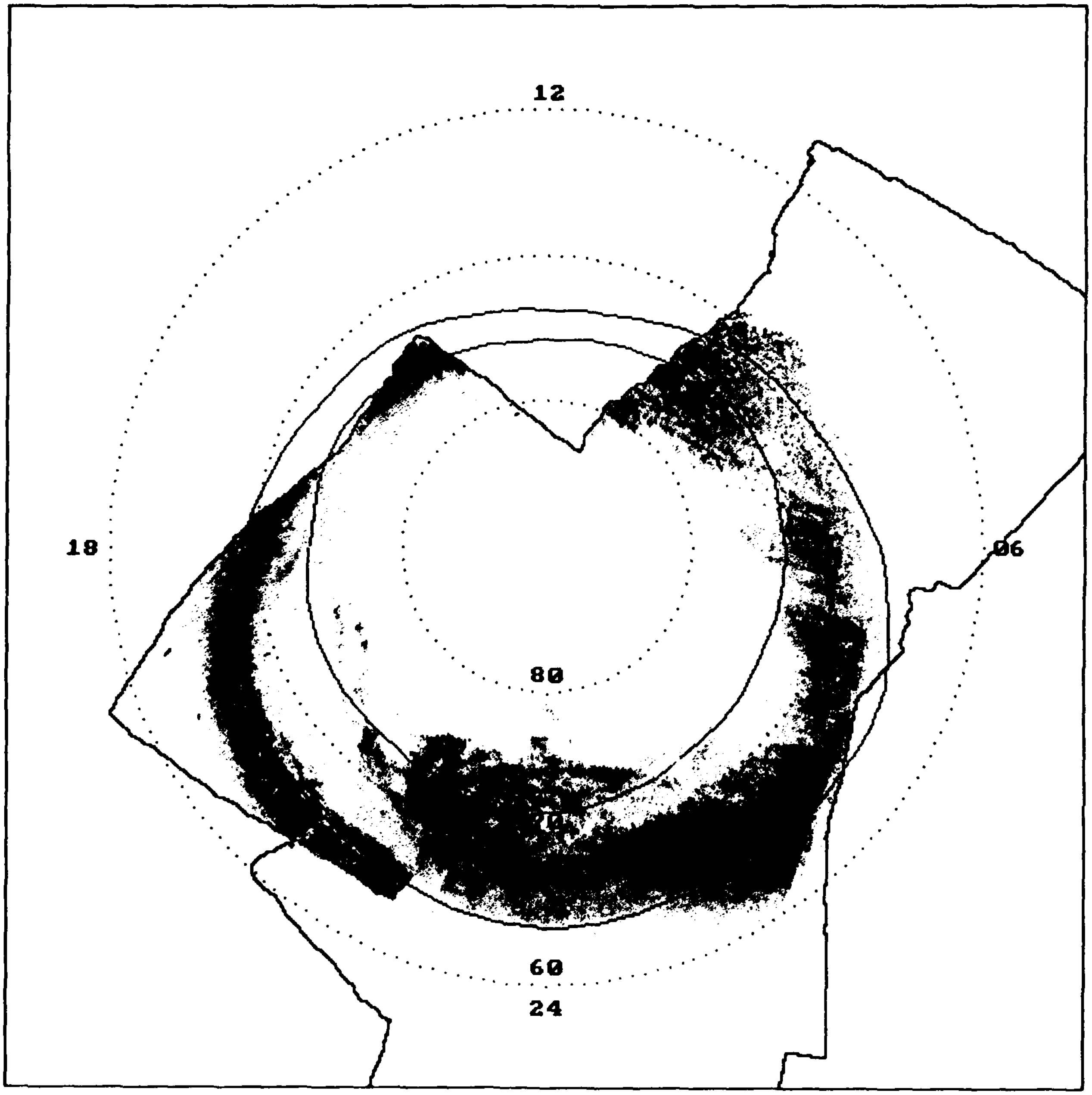

Figure .33: Average auroral intensity - $K_p = 3$, $\lambda = 1356\AA$.

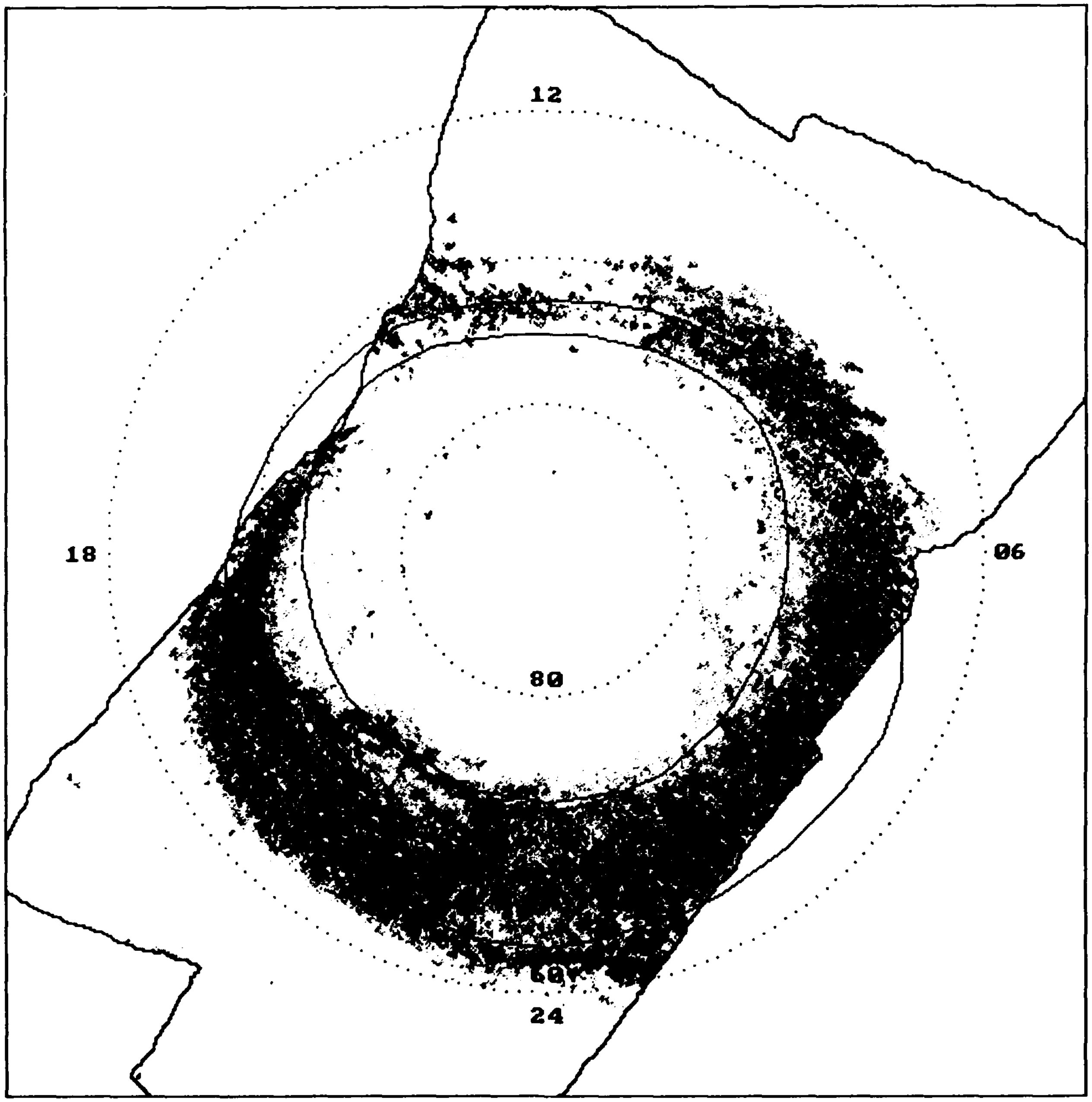

Figure .34: Average auroral intensity - $K_p = 4$, $\lambda = 1596\AA$.

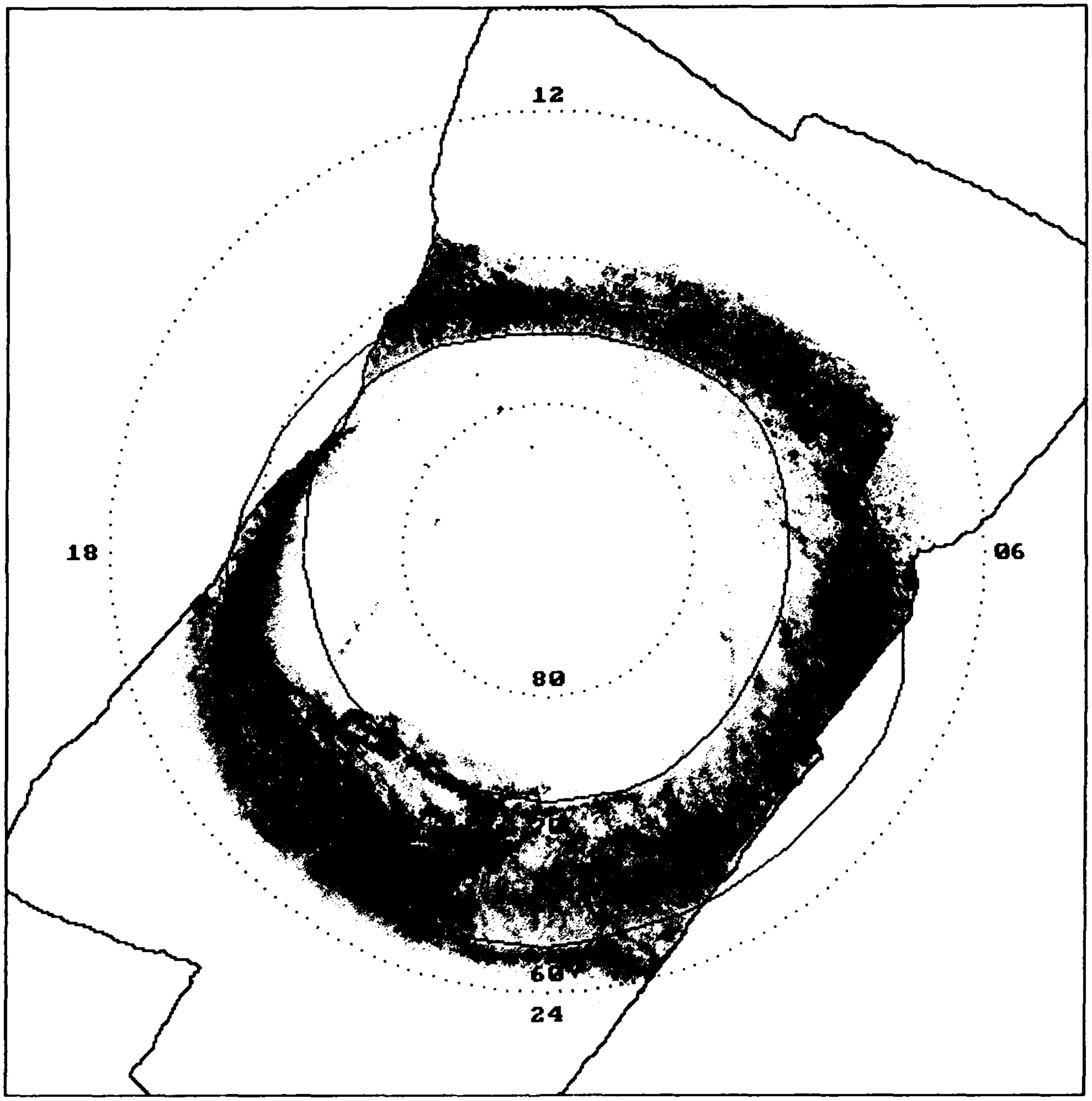

Figure .35: Average auroral intensity - $K_p = 4$, $\lambda = 1356\AA$.

.7.2 Future Research

This report summarizes the first two years of research on image processing of the Polar BEAR data. The software has matured to a complete package for the pre-processing, geometric and photometric calibration, and post-processing of AIRS images.

Figures 16–35 of this report depict first results of a project recently initiated utilizing the above package. Our aim is to create a complete and comprehensive set of maps of auroral frequency and average brightness in the far ultraviolet as a function of geomagnetic activity indices. The semiautomatic nature of the image-processing routines will allow us to enlarge the small sample (~ 40 scenes) to create a statistically valid database (~ 50 scenes per K_p group) for the above maps.

We will correlate known geomagnetic activity indices, such as IMF and K_p, with the well-resolved discrete arcs which are immersed in the continuous aurora. The sensitivity of at least one of the detectors (1356Å) affords us to study and compare the magnetic latitudinal and longitudinal distribution of the localized arcs with the continuous aurora. Basic attributes of the aurora, such as intensity, dimensional morphology, and occurrence probability, will be quantitatively examined.

Recently, the daylight aurora has captured the imagination of many researchers. Polar BEAR images, processed with the package we have developed, present an unmatchable opportunity for the study of this unique and unexplored territory. The airglow subtraction technique allows one to study daylight aurora without the interfering background radiation. Furthermore, relations between airglow indices such as solar flux, geomagnetic coordinates, and electron densities may permit true geographic-coordinate mapping of electron density profiles.

Bibliography

[1] Chapman, B. S., The absorption and dissociative or ionising effect of monochromatic radiation in an atmosphere on a rotating earth, *Proc. Phys. Soc., 43*, 26 and 483, 1931.

[2] DelGreco, F. P., Huffman, R. E., Larrabee, J. C., Eastes, R. W., LeBlanc, F. J., and Meng, C. -I., Organizing and Utilising the Imaging and Spectral Data from Polar BEAR, *Ultraviolet Technology, Proc. SPIE*, 1988.

[3] Feldstein, Y. I., and Starkov, G. V., Dynamics of Auroral Belt and Polar Geomagnetic Disturbances, *Planet. Space Sci., 15*, 209, 1967.

[4] Feldstein, Y. I., and Galperin, Yu. I., The auroral luminosity structure in the high-latitude upper atmosphere: its dynamics and relationship to the large-scale structure of the earth's magnetosphere, *Rev. Geophys., 23*, 217, 1985.

[5] Fremouw, E. J., Rino, C. L., Huffman, R. E., Rich, F. J., Meng, C. - I., Potocki, K. A., Potemra, T. A., Hanson, W. B., Heelis, R. A., and Wittwer, L. A., The HILAT program, *EOS, 64*, 163, 1983.

[6] Gustafsson, G., A revised corrected geomagnetic coordinate system, *Arkiv för Geofysik, 5*, 595, 1969.

[7] Hakura, Y., Tables and maps of geomagnetic coordinates corrected by the higher order spherical harmonic terms, *Rep. Ions. Sp. Res. Japan, 19*, 121, 1965.

[8] Huffman, R. E., Larrabee, J. C., and LeBlanc, F. J., UV Remote Sensing of the Aurora and Ionosphere for C^3I system use, *Radio Science, 20*, 425, 1985.

[9] Hultqvist, B., The geomagnetic field lines in higher approximation, *Arkiv för Geofysik, 3*, 63, 1958.

[10] Kasachevskaya, T. V., and Ivanov-Kholodnyy, G. S., Rocket data on the behavior of electron concentration in the ionosphere at heights of 100–300 km, *Geomagn. i aeronomiya*, 1965.

[11] Meng, C. -I., and Huffman, R. E., Ultraviolet Imaging from Space of the Aurora under Full Sunlight, *Geophys. Res. Lett., 11*, 315, 1984.

[12] Osnovich., I., and Tur, M., Polar BEAR UV Images of Airglow and Aurora - Data Reduction and Analysis, *Annual Technical Report to NorthWest Research Ass.*, Sep. 1988. GL-TR-89-0177, ADA214203

[13] Osnovich, I., and Tur, M., Stabilising the Polar BEAR Retrospectively, *Research Progress and Forecast Report to AFGL*, Jan. 1989.

[14] Ravits, A., UV Aurora mapping in corrected geomagnetic coordinates, M.Sc. thesis, Fac. of Engineering, Tel Aviv University, Tel Aviv, 1989.

[15] Rosenberg, N., UV Airglow and Aurora Maps from the AIM UV Imager, *Final Report to Computational Physics Inc.*, July 1986.

[16] Rosenberg, N., and Quesada, A. F., Satellite UV Image Processing, *Ultraviolet Technology, Proc. SPIE*, 1988.

[17] Schenkel, F. W., Ogorsalek, B. S., Larrabee, J. C., LeBlanc, F. J., and Huffman, R. E., UV Daytime Auroral and Ionospheric imaging from Space, *Applied Optics, 24*, 3395, 1985.

[18] Schenkel, F. W., Ogorsalek, B. S., Gardner, R. R., Hutchins, R. A., Huffman, R. E., and Larrabee, J. C., Simultaneous Multi-Spectral Narrow Band Auroral Imagery from Space (1150A to 6300A), *Ultraviolet Technology, Proc. SPIE*, 687, 1986.

[19] Sommerville, The elements of non-Euclidean geometry, New York, Dover, 1958.

[20] Strickland, D. J., and Anderson, D. E., Radiation transport effects on the OI 1356Å limb intensity profile in the dayglow, *J. Geophys. Res., 88*, 9260, 1983.

[21] Swider, W. J., The determination of the optical depth at large solar zenith distances, *Planet. Space Sci., 12*, 761, 1964.

[22] Whalen, J. A., Auroral oval plotter and monographs for determining corrected geomagnetic local time, latitude, and longitude for high latitude in the northern hemisphere, 1970.

[23] Wilkes, M. V., A table of Chapman's grasing incidence integral $Ch(\chi, X)$, *Proc. Phys. Soc., 67B*, 304, 1954.